Reviews in Mineralogy & Geochemistry
Vol. 78 pp. 33-74, 2014

Fundamentals of XAFS

Matthew Newville

Center for Advanced Radiation Sources
University of Chicago
Chicago, Illinois 60637, U.S.A.

newville@cars.uchicago.edu

The basic physical principles of X-ray Absorption Fine-Structure (XAFS) are presented. XAFS is an element-specific spectroscopy in which measurements are made by tuning the X-ray energy at and above a selected core-level binding energy of a specified element. Although XAFS is a well-established technique providing reliable and useful information about the chemical and physical environment of the probe atom, its requirement of an energy-tunable X-ray source means it is primarily done with synchrotron radiation sources and so is somewhat less common than other spectroscopic analytical methods. XAFS spectra are especially sensitive to the oxidation state and coordination chemistry of the selected element. In addition, the extended oscillations of the XAFS spectra are sensitive to the distances, coordination number and species of the atoms immediately surrounding the selected element. This Extended X-ray Absorption Fine-Structure (EXAFS) is the main focus of this chapter. As it is element-specific, XAFS places few restrictions on the form of the sample, and can be used in a variety of systems and bulk physical environments, including crystals, glasses, liquids, and heterogeneous mixtures. Additionally, XAFS can often be done on low-concentration elements (typically down to a few ppm), and so has applications in a wide range of scientific fields, including chemistry, biology, catalysis research, material science, environmental science, and geology. Special attention in this chapter is given to the basic concepts used in analysis and modeling of EXAFS spectra.

INTRODUCTION

X-ray absorption fine structure (XAFS) is the modulation of an atom's X-ray absorption probability at energies near and above the binding energy of a core-level electron of the atom. The XAFS is due to the chemical and physical state of the absorbing atom. XAFS spectra are especially sensitive to the formal oxidation state, coordination chemistry, and the distances, coordination number and species of the atoms immediately surrounding the selected element. Because of this sensitivity, XAFS provides a practical and relatively simple way to determine the chemical state and local atomic structure for a selected atomic species, and is used routinely in a wide range of scientific fields, including biology, environmental science, catalysts research, and material science. Since XAFS is an atomic probe, there are few constraints on the form of the samples that can be studied, and it can be used in a variety of systems and sample environments.

All atoms have core level electrons, and XAFS spectra can be measured for essentially every element on the periodic table. Importantly, crystallinity is not required for XAFS measurements, making it one of the few structural probes available for noncrystalline and highly disordered materials, including ions dissolved in solutions. Because X-rays are fairly penetrating in matter, XAFS is not inherently surface-sensitive, though special measurement techniques can be applied to enhance its surface sensitivity. Intense X-ray sources can make

1529-6466/14/0078-0002$05.00 http://dx.doi.org/10.2138/rmg.2014.78.2

very small beams, allowing XAFS to be done on samples as small as a few square microns. In addition, many variations on experimental techniques and sample conditions are available for XAFS, including *in situ* chemical processes and extreme conditions of temperature and pressure. XAFS measurements can be made on elements of minority and even trace abundance in many systems, giving a unique and direct measurement of chemical and physical state of dilute species in a variety of systems.

X-ray absorption measurements are relatively straightforward, provided one has an intense and energy-tunable source of X-rays. In practice, this usually means the use of synchrotron radiation, and the history and development of XAFS closely parallels that of synchrotron sources. Since the characteristics of synchrotron sources and experimental station dictate what energy ranges, beam sizes, and intensities are available, this often puts practical experimental limits on the XAFS measurements that can be done at a particular station, even if there are few inherent limits on the XAFS technique itself.

Though XAFS measurements can be straightforward, a complete understanding of XAFS involves a wonderful mixture of modern physics and chemistry and a complete mastery of the data analysis can be somewhat challenging. Though the basic phenomena is well-understood, an accurate theoretical treatment is fairly involved and, in some respects still an area of active research. The interpretation and analysis of XAFS is not always straightforward, though significant progress has been made in both the theoretical and analytical tools for XAFS in the past few decades. Accurate and precise interpretation of XAFS spectra is routine, if not always trivial for novice experimentalists.

The X-ray absorption spectrum is typically divided into two regimes: X-ray absorption near-edge spectroscopy (XANES) and extended X-ray absorption fine-structure spectroscopy (EXAFS). Though the two have the same physical origin, this distinction is convenient for the interpretation. XANES is strongly sensitive to formal oxidation state and coordination chemistry (e.g., octahedral, tetrahedral coordination) of the absorbing atom, while the EXAFS can be used to determine the distances, coordination number, and species of the neighbors of the absorbing atom.

XAFS is a mature technique, with a literature spanning many decades and many disciplines. As a result, several books (Teo 1986; Koningsberger and Prins 1988; Bunker 2010; Calvin 2013) have been written specifically about XAFS, and one book on X-ray physics (Als-Nielsen and McMorrow 2001) covers XAFS in some detail. There have been many chapters and review articles written about XAFS, including early reviews of the fledgling technique (Stern and Heald 1983), complete theoretical treatments (Rehr and Albers 2000), and reviews focusing on applications in a variety of fields, including mineralogy (Brown et al. 1988) and soil science (Kelly et al. 2008). Earlier review articles on applications of synchrotron techniques in geochemistry and environmental science (Manceau et al. 2002; Sutton et al. 2002) also contain considerable information about XAFS. In addition, several on-line resources (XAFS.ORG 2003; IXAS 2012) have lengthy tutorials and links to software packages and documentation for XAFS. It is not possible or particularly useful to give a full review of the XAFS literature, even restricting to a single field such as geochemistry or mineralogy.

In this work, the origins and interpretations of XAFS will be introduced, with a hope of aiding the reader to be able to make high-quality XAFS measurements as well as process and analyze the data. The emphasis here is particularly on the processing and analysis of the extended oscillations of the XAFS spectra, as the near-edge portion of the spectra is covered in more detail elsewhere. This chapter will not make one an expert in XAFS, but it should provide a firm foundation for a new practitioner of XAFS. The above citations are all strongly recommended reading for further insights and different perspectives and emphasis. The reader is not expected to have previous experience with XAFS or X-ray measurements, but some

familiarity with advanced undergraduate-level chemistry or physics and a knowledge of experimental practices and data interpretation will be helpful.

X-RAY ABSORPTION AND FLUORESCENCE

X-rays are light with energies ranging from about 500 eV to 500 keV, or wavelengths from about 25 Å to 0.25 Å. In this energy regime, light is absorbed by all matter through the *photoelectric effect*, in which an X-ray photon is absorbed by an electron in a tightly bound quantum core level (such as the 1*s* or 2*p* level) of an atom, as shown in Figure 1.

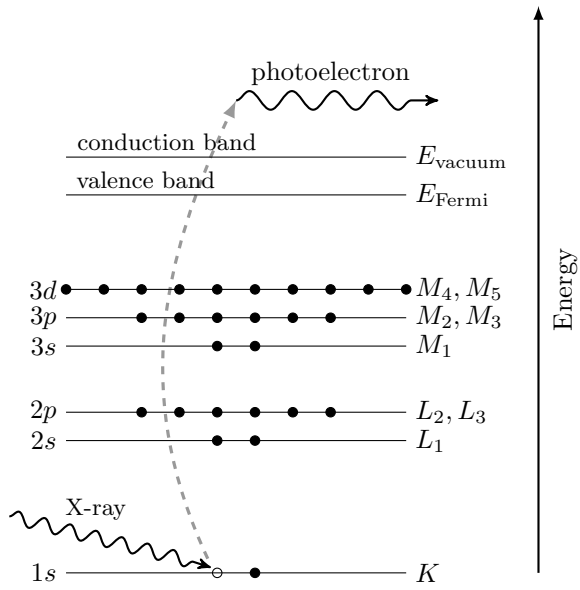

Figure 1. The photoelectric effect, in which an X-ray is absorbed by an atom and a core-level electron is promoted out of the atom, creating a photoelectron and leaving behind a hole in the core electron level.

In order for a particular electronic core level to absorb the X-ray, its binding energy must be less than the energy of the incident X-ray. If the binding energy is greater than the energy of the X-ray, the bound electron will not be perturbed from the well-defined quantum state and will not absorb the X-ray. If the binding energy of the electron is less than that of the X-ray, the electron may be removed from its quantum level. In this case, the X-ray is destroyed (that is, absorbed) and any energy in excess of the electronic binding energy is given to a photoelectron that is ejected from the atom. This process has been well understood for more than a century (Einstein received the Nobel Prize for describing this effect). As we will see, the full implications of this process when applied to molecules, liquids, and solids will give rise to XAFS.

When discussing X-ray absorption, we are primarily concerned with the *absorption coefficient*, μ which gives the probability that X-rays will be absorbed according to the Beer-Lambert Law:

$$I = I_0 e^{-\mu t} \tag{1}$$

where I_0 is the X-ray intensity incident on a sample, t is the sample thickness, and I is the

intensity transmitted through the sample, as shown in Figure 2. For X-rays of sufficiently low intensity, the X-ray intensity is proportional to the number of X-ray photons—we will ignore any non-linear or strong field effects here, and consider only the case of absorption by an otherwise unperturbed atom.

At most X-ray energies, the absorption coefficient μ is a smooth function of energy, with a value that depends on the sample density ρ, the atomic number Z, atomic mass A, and the X-ray energy E roughly as

$$\mu \approx \frac{\rho Z^4}{AE^3} \tag{2}$$

The strong dependence of μ on both Z and E is a fundamental property of X-rays, and is the key to why X-ray absorption is useful for medical and other imaging techniques such as X-ray computed tomography. Figure 3 shows the energy-dependence of μ/ρ described in Equation (2) for O, Fe, Cd, and Pb in the normal X-ray regime of 1 to 100 keV. The values span several orders of magnitude, so that good contrast between different materials can be achieved for nearly any sample thickness and concentrations by adjusting the X-ray energy.

When the incident X-ray has an energy equal to that of the binding energy of a core-level electron, there is a sharp rise in absorption: an *absorption edge* corresponding to the promotion of the core level to the continuum. For XAFS, we are concerned with the energy dependence of μ at energies near and just above these absorption edges. An XAFS measurement is then simply a measure of the energy dependence of μat and above the binding energy of a known core level of a known atomic species. Since every atom has core-level electrons with well-defined binding energies, we can select the element to probe by tuning the X-ray energy to an appropriate absorption edge. These absorption edge energies are well-known (usually to within a tenth of percent),

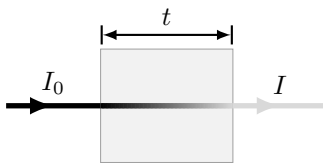

Figure 2. X-ray absorption and the Beer-Lambert law: An incident beam of monochromatic X-rays of intensity I_0 passes through a sample of thickness t, and the transmitted beam has intensity I. The absorption coefficient μ is given by the Beer-Lambert law, $I = I_0 e^{-\mu t}$.

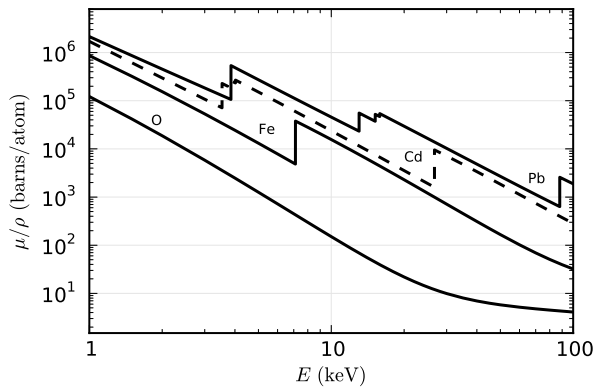

Figure 3. The absorption cross-section μ/ρ for several elements over the X-ray energy range of 1 to 100 keV. Notice that there are at least 5 orders of magnitude in variation in μ/ρ, and that in addition to the strong energy dependence, there are also sharp jumps in cross-section corresponding to the core-level binding energies of the atoms.

and tabulated. The edge energies vary with atomic number approximately as Z^2, and both *K* and *L* levels can be used in the hard X-ray regime (in addition, *M* edges can be used for heavy elements in the soft X-ray regime), which allows most elements to be probed by XAFS with X-ray energies between 4 and 35 keV, as shown in Figure 4. Because a particular absorption edge of the element of interest is chosen in the experiment, XAFS is *element-specific*.

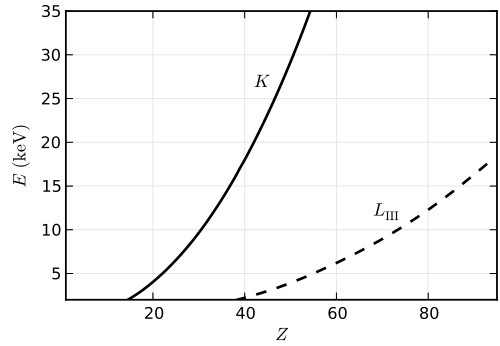

Figure 4. The energies for the X-ray *K* and L_{III} absorption edges as a function of atomic number *Z*. The energies follow $E \sim Z^2$, and all elements with $Z > 20$ have an X-ray edge above 4 keV.

Following an absorption event, the atom is said to be in an *excited state*, with one of the core electron levels left empty (a so-called *core hole*), and a *photoelectron* emitted from the atom. The excited state will eventually decay (typically within a few femtoseconds) of the absorption event. Though this decay does not affect the X-ray absorption process, it is important for the discussion below.

There are two main mechanisms for the decay of the excited atomic state following an X-ray absorption event, as shown in Figure 5. The first of these is X-ray fluorescence, in which a higher energy electron core-level electron fills the deeper core hole, ejecting an X-ray of well-defined energy. The fluorescence energies emitted in this way are characteristic of the atom, and can be used to identify the atoms in a system, and to quantify their concentrations. For example, an *L* shell electron dropping into the *K* level gives the K_α fluorescence line.

The second process for de-excitation of the core hole is the Auger effect, in which an electron drops from a higher electron level and a second electron is emitted into the continuum

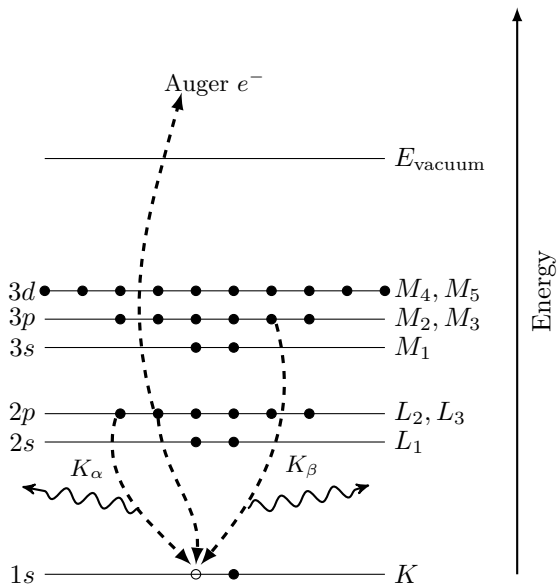

Figure 5. The excited atomic state will decay by either X-ray fluorescence or the Auger effect. In either case, an electron is moved from a less tightly bound orbital to the empty core level, and the energy difference between these levels is given to the emitted particle (X-ray or electron). The emission energies have precise values that are characteristic for each atom, and can be used to identify the absorbing atom. Though the probability of whether the decay occurs by fluorescence or Auger emission depends on the atomic number *Z* and energy-level, the probability of emission is directly proportional to the absorption probability, and so can be used to measure EXAFS and XANES.

(and possibly even out of the sample). In either case, a cascade of subsequent emissions will fill the newly formed, less tightly bound hole until the atom is fully relaxed. Either of these processes can be used to measure the absorption coefficient μ, though the use of fluorescence is somewhat more common. In the hard X-ray regime (> 10 keV), X-ray fluorescence is more likely to occur than Auger emission, but for lower energies Auger emission dominates.

XAFS can be measured in two different modes. In transmission mode, the intensity of an X-ray beam is sampled before and after being transmitted through a sample, as shown in Figure 2. In fluorescence mode, a secondary emission resulting from the absorption of the X-ray is measured, such as X-ray fluorescence or Auger electrons just mentioned, or in some cases even by monitoring visible light emitted by a sample as part of the cascade of decay events. We will return to the details of the measurements later, but for now it is enough to say that we can measure the energy dependence of the X-ray absorption coefficient μ(*E*) either in transmission mode as

$$\mu(E) = \ln\left(\frac{I_0}{I}\right)$$

or in fluorescence (or emission) mode as

$$\mu(E) \propto \frac{I_f}{I_0}$$

where I_f is the monitored intensity of a fluorescence line (or electron emission) associated with the absorption process.

A typical XAFS spectrum (measured in the transmission geometry for a powder of FeO) is shown in Figure 6. The sharp rise in μ(*E*) due to the Fe 1s electron level (near 7112 eV) is clearly visible in the spectrum, as are the oscillations in μ(*E*) that continue well past the edge. As mentioned in the introduction, the XAFS is generally thought of in two distinct portions: the near-edge spectra (XANES)—typically within 30 eV of the main absorption edge, and the extended fine-structure (EXAFS), which can continue for a few keV past the edge. As we shall see, the basic physical description of these two regimes is the same, but some important approximations and limits allow us to interpret the extended portion of the spectrum in a simpler and more quantitative way than is currently possible for the near-edge spectra.

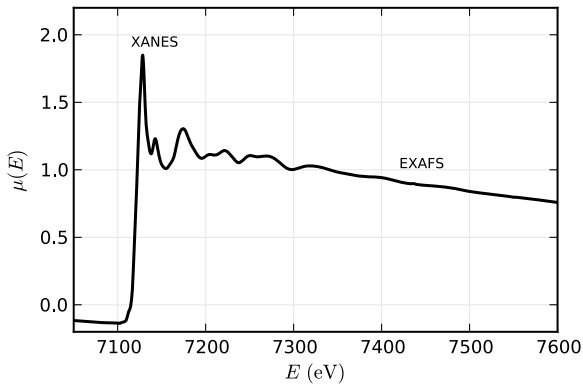

Figure 6. XAFS μ(E) for the Fe K edge of FeO, showing the near-edge (XANES) region and the extended fine structure (EXAFS).

For the EXAFS, we are interested in the oscillations well above the absorption edge, and define the EXAFS fine-structure function $\chi(E)$ as a change to $\mu(E)$, as

$$\mu(E) = \mu_0(E)\left[1 + \chi(E)\right] \tag{3}$$

where $\mu(E)$ is the measured absorption coefficient, $\mu_0(E)$ is a smooth background function representing the absorption of an isolated atom. The isolated XAFS is usually written as

$$\chi(E) = \frac{\mu(E) - \mu_0(E)}{\Delta\mu} \tag{4}$$

where $\Delta\mu$ is the measured jump in the absorption $\mu(E)$ at the threshold energy. Note that, due primarily to experimental considerations, XAFS is generally normalized by the energy-independent edge jump rather than an energy-dependent $\mu_0(E)$.

As we will see, EXAFS is best understood in terms of the wave behavior of the photoelectron created in the absorption process. Because of this, it is common to convert the X-ray energy to k, the wave number of the photoelectron, which has dimensions of 1/distance and is defined as

$$k = \sqrt{\frac{2m(E - E_0)}{\hbar^2}} \tag{5}$$

where E_0 is the absorption edge energy, m is the electron mass, and $\hbar$ is Planck's constant. The primary quantity for EXAFS is then $\chi(k)$, the isolated variation in absorption coefficient as a function of photoelectron wave number, and $\chi(k)$ is often referred to simply as "the EXAFS." The EXAFS extracted from the Fe *K*-edge for FeO is shown in Figure 7 (left). The EXAFS is clearly oscillatory, and also decays quickly with k. To emphasize the oscillations, $\chi(k)$ is often multiplied by a power of k typically k^2 or k^3 for display, as is done for the plot in Figure 7.

The different frequencies apparent in the oscillations in $\chi(k)$ correspond to different near-neighbor coordination shells. This can be seen most clearly by applying a Fourier transform to the data, converting the data from depending on wavenumber k to depending on distance R. As seen in the right panel of Figure 7, the oscillations present in the EXAFS $\chi(k)$ give rather well-defined peaks as a function of R. Though these peaks are not at the exact distances from the absorbing atom to its near neighbors, they are due to the neighboring atoms being at particular distances, and the values for the near neighbor distances can be accurately determined from the EXAFS oscillations.

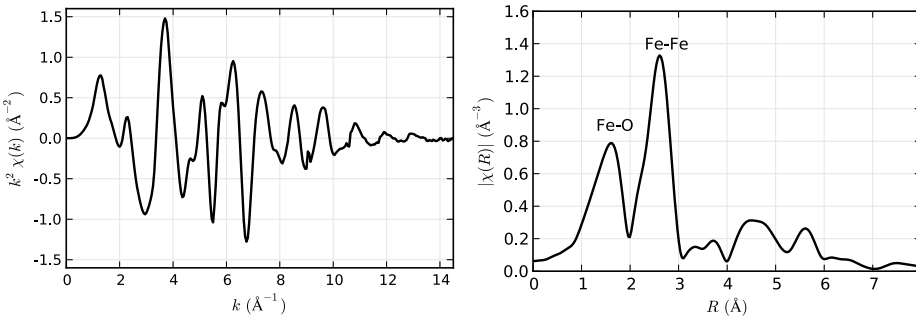

Figure 7. Isolated EXAFS for the Fe K edge of FeO, shown weighted by k^2 (*left*) to emphasize the high-k portion of the spectrum, and the Fourier transform of the k-weighted XAFS, $\chi(R)$ (*right*), showing the contribution from Fe-O and Fe-Fe neighbors.

A remarkable feature of EXAFS is that the contributions to the EXAFS from scattering from different neighboring atoms can be described by a relatively straightforward *EXAFS Equation*, a simplified form of which is

$$\chi(k) = \sum_j \frac{N_j f_j(k) e^{-2k^2\sigma_j^2}}{kR_j^2} \sin\left[2kR_j + \delta_j(k)\right]$$

Here $f(k)$ and $\delta(k)$ are scattering properties of the photoelectron emitted in the absorption process by the atoms neighboring the excited atom, N is the number of neighboring atoms, R is the distance to the neighboring atom, and σ^2 is the disorder in the neighbor distance. Though slightly complicated, the EXAFS equation is simple enough to enable us to model EXAFS data reliably, and so determine N, R, and σ^2 once we know the scattering amplitude $f(k)$ and phase-shifts $\delta(k)$. Furthermore, because these scattering factors depend on the Z of the neighboring atom, EXAFS is also sensitive to the atomic species of the neighboring atom.

A SIMPLE THEORETICAL DESCRIPTION OF XAFS

In this section, a simple physical description of the XAFS process and the origin of the EXAFS Equation will be given. Other useful treatments on a similar level can be found in other places (Stern 1988; Rehr and Albers 2000) as well. As in the previous section, we start with the photoelectric effect, now shown in Figure 8, in which an X-ray of energy E is absorbed by a core-level electron of a particular atom with binding energy E_0. Any energy from the X-ray in excess of this binding energy is given to a photoelectron that propagates away from the absorbing atom. We will treat the photoelectron as a wave, noting that its wavelength is proportional to $1/\sqrt{E-E_0}$. It is most common to describe the photoelectron by its *wavenumber*, $k = 2\pi/\lambda$, given in Equation (5).

The absorption of the X-ray by the particular core electron level requires there to be an *available quantum state* for the ejected photoelectron to go to. If no suitable state is available, there will be no absorption from that core level. At X-ray energies below the 1*s* binding energy (for example, below 7.1 keV for iron) the 1*s* electron could only be promoted to a valence electron level below the Fermi level—there is simply not enough energy to put the electron into the conduction band. Since all the valence levels are filled, there is no state for the 1*s* electron to fill, and so there is no absorption from that core-level. Of course, a sample is not transparent to X-rays with energies below the 1s binding level, as the higher level electrons can be promoted into the continuum, but there is a sharp jump in the probability of absorption as the X-ray energy is increased above a core level binding energy. In fact, these binding levels are often referred to as absorption edges due to this strong increase in absorption probability.

It should be noted that the quantum state that the photoelectron occupies has not only the right energy, but also the right angular momentum. For photo-electric absorption, the angular momentum number must change by 1, so that an *s* core-level is excited into a *p* state, while a *p* core-level can be excited into either an *s* or *d* level. This is important for a detailed, quantitative description of the XAFS, but is not crucial to basic discussion of XAFS here, as we are generally dealing with energies far above the continuum which have large density of states. On the other hand, the momentum state can be extremely important when considering XANES, the near-edge portion of the spectra, as the available energy states of the unfilled anti-bonding orbitals still have well-defined and specific angular momentum states above the continuum level.

The picture above described absorption for an isolated atom. When a neighboring atom is included (Fig. 9), the photoelectron can scatter from the electrons of this neighboring atom, and some part of the scattered photoelectron can return to the absorbing atom. Of course, the

simple one-dimensional picture shown above suggests that the probability of scattering the photoelectron by the neighboring atom is quite large. In a real, three dimensional sample, the photoelectron wavefunction spreads radially out and has a lower probability of scattering from the electrons in the neighboring atoms. The important point is that some portion of the photoelectron wavefunction is scattered from the neighboring atom, and returns to the absorbing atom, all in a single coherent quantum state. Since the absorption coefficient depends on whether there is an available, unfilled electronic state at the location of the atom and at the

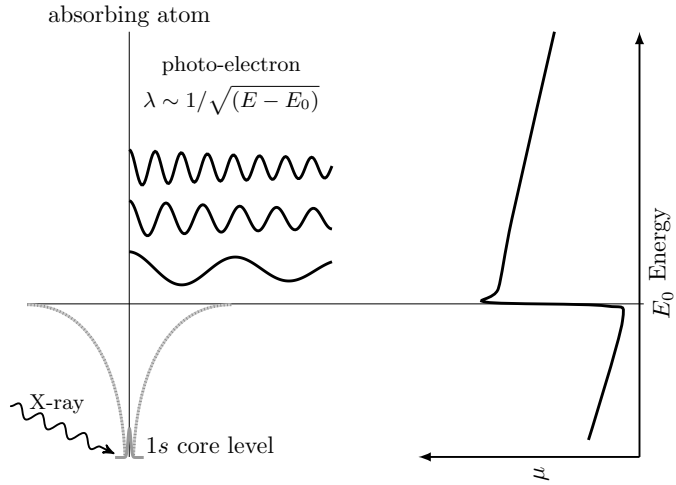

Figure 8. Cartoon of X-ray absorption through the photoelectric process. As the energy of the X-rays is increased to just above the energy of a tightly bound core electron level, E_0, the probability of absorption has a sharp rise—an edge jump. In the absorption process, the tightly bound core-level is destroyed, and a photoelectron is created. The photoelectron travels as a wave with wavelength proportional to $1/(E - E_0)^{1/2}$.

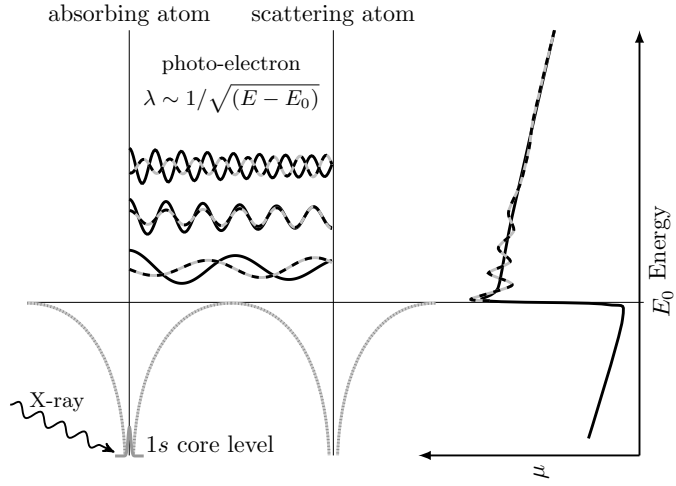

Figure 9. XAFS occurs because the photoelectron can scatter from a neighboring atom. The scattered photoelectron can return to the absorbing atom, modulating the amplitude of the photoelectron wave-function at the absorbing atom. This in turn modulates the absorption coefficient $\mu(E)$, causing the EXAFS.

appropriate energy (and momentum), the presence of the photoelectron scattered back from the neighboring atom will alter the absorption coefficient: This is the origin of XAFS.

A rough explanation of the EXAFS equation

We'll now spend some effort developing the standard EXAFS equation using a slightly more formal description of this simple physical picture above, but still somewhat less rigorous than a full-blown quantum mechanical description. The goal here is to describe enough of the basic physics to identify where the different components of the EXAFS equation arise from, and so what they mean for use in the analysis of spectra.

Since X-ray absorption is a *transition* between two quantum states (from an initial state with an X-ray, a core electron, and no photoelectron to a final state with no X-ray, a core hole, and a photoelectron), we describe $\mu(E)$ with Fermi's Golden Rule:

$$\mu(E) \propto \left|\langle i|H|f\rangle\right|^2 \tag{6}$$

where $\langle i|$ represents the initial state (an X-ray, a core electron, and no photoelectron), $|f\rangle$ is the final state (no X-ray, a core hole, and a photoelectron), and H is the interaction term, which we'll come back to shortly. Since the core-level electron is very tightly bound to the absorbing atom, the initial state will not be altered by the presence of the neighboring atom, at least to first approximation. The final state, on the other hand, will be affected by the neighboring atom because the photoelectron will be able to scatter from it. If we expand $|f\rangle$ into two pieces, one that is the "bare atom" portion ($|f_0\rangle$), and one that is the effect of the neighboring atom ($|f\rangle$) as

$$|f\rangle = |f_0\rangle + |\Delta f\rangle$$

We can then expand Equation (6) to

$$\mu(E) \propto \left|\langle i|H|f_0\rangle\right|^2 \left[1 + \langle i|H|\Delta f\rangle \frac{\langle f_0|H|i\rangle^*}{\left|\langle i|H|f_0\rangle\right|^2} + C.C.\right]$$

where C.C. means complex conjugate. We've arranged the terms here so that this expression resembles Equation (3),

$$\mu(E) = \mu_0(E)\left[1 + \chi(E)\right]$$

We can now assign $\mu_0 = \left|\langle i|H|f_0\rangle\right|^2$ as the "bare atom absorption," which depends only on the absorbing atom—as if the neighboring atom wasn't even there. We can also see that the fine-structure χ will be proportional to the term with $|f\rangle$:

$$\chi(E) \propto \langle i|H|\Delta f\rangle$$

which indicates that the EXAFS is due to the interaction of the scattered portion of the photoelectron and the initial absorbing atom.

We can work out this term for χ as an integral equation fairly easily, if approximately. The interaction term H represents the process of changing between two states of given energy and momentum. In quantum radiation theory, the interaction term needed is the $p \cdot A$ term, where A is the quantized vector potential (there is also an $A \cdot A$ term, but this does not contribute to absorption). For the purposes here, this reduces to a term that is proportional to e^{ikr}. The initial state is a tightly bound core-level, which we can approximate by a delta function (a 1s level for atomic number Z extends to around a_0/Z, where a_0 is the Bohr radius of ≈ 0.529 Å, so this is a good approximation for heavy elements, but less good for very light elements). The change in final state is just the wave-function of the scattered photoelectron, $\psi_{scatter}(r)$. Putting these terms together gives a simple expression for the EXAFS:

$$\chi(E) \propto \int dr\delta(r)e^{ikr}\psi_{\text{scatter}}(r) = \psi_{\text{scatter}}(0) \tag{7}$$

In words, this simply states the physical picture shown in Figure 9:

The EXAFS $\chi(E)$ is proportional to the amplitude of the scattered photoelectron at the absorbing atom.

We can now evaluate the amplitude of the scattered photoelectron at the absorbing atom to get the EXAFS equation. Using the simple physical picture from Figure 9, we can describe the outgoing photoelectron wave-function (k, r) traveling as a spherical wave,

$$\psi(k,r) = \frac{e^{ikr}}{kr} \tag{8}$$

traveling a distance R to the neighboring atom, then scattering from a neighbor atom, and traveling as a spherical wave a distance R back to the absorbing atom. We simply multiply all these factors together to get

$$\chi(k) \propto \psi_{\text{scatter}}(k, r=0) = \frac{e^{ikR}}{kR}\left[2kf(k)e^{i\delta(k)}\right]\frac{e^{ikR}}{kR} + C.C.$$

where $f(k)$ and $\delta(k)$ are scattering properties of the neighboring atom, and C.C. means complex conjugate. As mentioned before, these scattering factors depend on the Z of the neighboring atom, as illustrated in Figure 10 for a few elements. Combining these terms in and using the complex conjugate to make sure we end up with a real function, we get

$$\chi(k) = \frac{f(k)}{kR^2}\sin\left[2kR + \delta(k)\right] \tag{9}$$

which looks much like the standard EXAFS equation. For mathematical convenience, the EXAFS Equation is sometimes written with the sin term replaced with the imaginary part of an exponential:

$$\chi(k) = \frac{f(k)}{kR^2}\text{Im}\left\{e^{i\left[2kR+\delta(k)\right]}\right\}$$

We'll use this form on occasion.

The treatment to get to Equation (9) was for one pair of absorbing atom and scattering atom, but for a real measurement we'll average over billions of X-ray absorption events and so atom pairs. Even for neighboring atoms of the same type, the thermal and static disorder in the bond distances will give a range of distances that will affect the XAFS. As a first approximation, the bonding environment and disorder will change the XAFS equation from Equation (9) to

$$\chi(k) = \frac{Nf(k)e^{-2k^2\sigma^2}}{kR^2}\sin\left[2kR + \delta(k)\right]$$

where N is the coordination number and σ^2 is the mean-square-displacement in the bond distance R. We'll return to this topic later.

Of course, real systems usually have more than one type of neighboring atom around a particular absorbing atom. This is easily accommodated in the XAFS formalism, as the measured XAFS will simply be a sum of the contributions from each scattering atom type or *coordination shell*:

$$\chi(k) = \sum_j \frac{N_j f_j(k)e^{-2k^2\sigma_j^2}}{kR_j^{\,2}}\sin\left[2kR_j + \delta_j(k)\right]$$

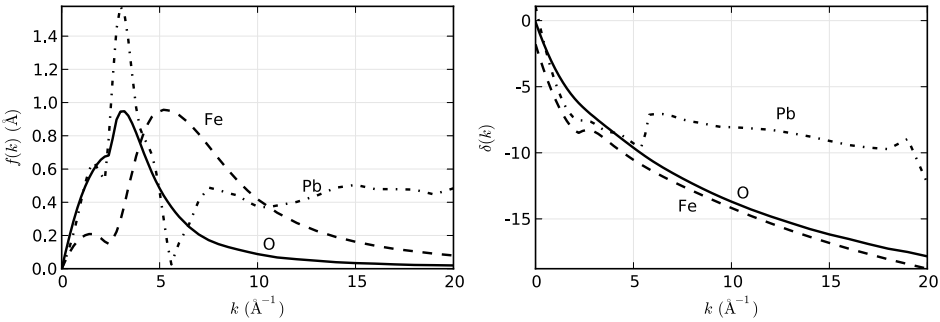

Figure 10. Functional forms for $f(k)$ (left) and $\delta(k)$ (right) for O, Fe, and Pb showing the dependence of these terms on atomic number Z. The variations in functional form allow Z to be determined (±5 or so) from analysis of the EXAFS.

where j represents the individual coordination shell of identical atoms at approximately the same distance from the central atom. In principle there can be many such shells, but as shells of similar Z become close enough (say, within a 0.05 Å of each other), they become difficult to distinguish from one another.

The explanation so far of what goes into the EXAFS equation gives the most salient features of the physical picture for EXAFS but ignores many nuances. In order to be able to quantitatively analyze EXAFS in real systems, we'll need to cover some of these subtleties, giving four main points to discuss. These are 1) the finite photoelectron mean free path, 2) the relaxation due to the passive (non-core) electrons of the excited atom, 3) multiple-scattering of the photoelectron, and 4) a more detailed treatment of structural and thermal disorder.

$\lambda(k)$: The inelastic mean free path

The most significant approximation we made above was to assert that the outgoing photoelectron went out as a spherical wave, as given in Equation (8). In doing so, we neglected the fact that the photoelectron can also scatter *inelastically* from other sources—other conduction electrons, phonons, and so on. In order to participate in the XAFS, the photoelectron has to scatter from the neighboring atom and return to the absorbing atom *elastically* (that is, at the same energy) as the outgoing photoelectron. In addition, the scattered portion of the photoelectron has to make it back to the absorbing atom before the excited state decays (that is, before the core hole is filled through the Auger or fluorescence process). To account for both the inelastic scattering and the finite *core-hole lifetime*, we can use a damped spherical wave:

$$\psi(k,r) = \frac{e^{ikr}e^{-r/\lambda(k)}}{kr}$$

for the photoelectron wave-function in place of the spherical wave of Equation (8). Here, λ is the *mean free path* of the photoelectron, representing how far it can typically travel before scattering inelastically or before the core hole is filled. The core-hole lifetime is on the order of 10^{-15} s, depending somewhat on the energy of the core-level. The mean free path is typically 5 to 30 Å and varies with k with a fairly universal dependence on k, shown in Figure 11. Including this $\lambda(k)$, the EXAFS equation becomes

$$\chi(k) = \sum_j \frac{N_j f_j(k) e^{-2R_j/\lambda(k)} e^{-2k^2\sigma_j^2}}{kR_j^{\,2}} \sin\left[2kR_j + \delta_j(k)\right]$$

It is the finite size of λ, as well as the $1/R^2$ term (which also originates from the wavefunction

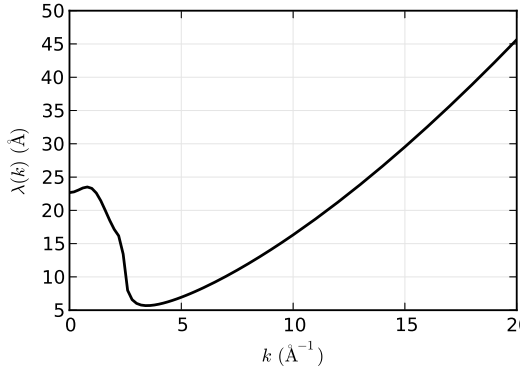

Figure 11. The photoelectron mean free path for XAFS, $\lambda(k)$, representing how far the photoelectron can travel and still participate in the XAFS. This term accounts for both the inelastic scattering of the photoelectron, and the finite lifetime of the core-hole.

of the outgoing photoelectron) in the EXAFS equation that shows EXAFS to be a local probe, insensitive to atomic structure beyond 10 Å or so.

As an aside, we note that it is possible to treat the losses that are described by $\lambda(k)$ as a complex wavenumber, so that k becomes $p = k + i/\lambda$, and the EXAFS Equation can be written with p instead of k. This reflects the common usage in the theoretical condensed matter physics literature that the photoelectron energy is complex, and so includes the effects of the mean free path not only in a $e^{-2R/\lambda}$ term, but also in the disorder terms, which can be important in some analyses. This can be incorporated into quantitative analysis tools, but is beyond the scope of the present work, so we will continue to use the form of the EXAFS Equation above, with the explicit λ term.

S_0^2: intrinsic losses

A second approximation we made in the description above was to ignore the relaxation due to the other electrons in the excited atom. That is, our "initial state" and "final state" above should have been for the entire atom, but we considered only a single core-level electron. Writing $\left|\Phi_0^{Z-1}\right\rangle$ for the remaining Z–1 electrons in unexcited atom, and $\left\langle\Phi_f^{Z-1}\right|$ for the Z–1 electrons in the excited atoms, we end up with a factor of

$$S_0^2 = \left|\left\langle\Phi_f^{Z-1}\middle|\Phi_0^{Z-1}\right\rangle\right|^2$$

that can be placed in front of the EXAFS equation. Though recent research has suggested that S_0^2 may have some k dependence, especially at low k, it is usually interpreted simply as a constant value, so that the EXAFS equation becomes

$$\chi(k) = \sum_j \frac{S_0^2 N_j f_j(k) e^{-2R_j/\lambda(k)} e^{-2k^2\sigma_j^2}}{kR_j^{\,2}} \sin\left[2kR_j + \delta_j(k)\right] \tag{10}$$

which is the final form of the EXAFS equation that we will use for analysis.

S_0^2 is assumed to be constant, and is generally found to be $0.7 < S_0^2 < 1.0$. By far the biggest consequence of this is that this factor is *completely correlated with N* in the EXAFS equation. This fact, along with the data reduction complication discussed later that the edge step $\Delta\mu$ in Equation (4) is challenging to determine experimentally, makes absolute values for the coordination number N difficult to determine with high accuracy.

Multiple scattering of the photoelectron

So far the treatment of EXAFS has implied that the photoelectron always scatters from one neighboring atom and returns to the absorber. In fact, the photoelectron can scatter from more than one neighboring atom, making a more convoluted *scattering path* than simply to one scattering atom and back. Examples of the more important types of multiple scattering paths are illustrated in Figure 12.

Multiple scattering paths can give important contributions for EXAFS, especially beyond the first coordination shell, and are often important for XANES. In general, most first-shell analysis of EXAFS is not strongly affected by multiple scattering, but second-shell analysis can be, and shells beyond the second are almost always complicated by multiple-scattering paths. For highly-ordered crystalline materials, focused linear multiple scattering paths, as shown Figure 12 can be particularly important, and neglecting them in an analysis can give erroneous results.

Though the details of the calculations are beyond the scope of this work (Rehr and Albers 2000), accounting for multiple scattering formally in the EXAFS equation is conceptually quite easy. We can simply change the meaning of the sum in Equation (10) to be a sum over *scattering paths*, including multiple scattering paths, instead of being a sum over coordination shells. We also have to change our interpretation of R from "interatomic distance" to "half path length." In addition, our scattering amplitudes $f(k)$ and phase-shifts $\delta(k)$ now need to include the contribution from each scattering atom in the path, so that the term in the EXAFS equation can be said to be *effective* scattering amplitudes and phase-shifts. Unfortunately, the existence of multiple scattering means that the number of paths needed to properly account for an EXAFS spectra grows quickly (exponentially) with path distance. This puts a practical limit on our ability to fully interpret EXAFS spectra from completely unknown systems.

Disorder terms and $g(R)$

We gave a simple description of disorder above, using $Ne^{-2k^2\sigma^2}$ in the EXAFS equation, where N is the coordination number and σ^2 is the mean-square displacement of the set of

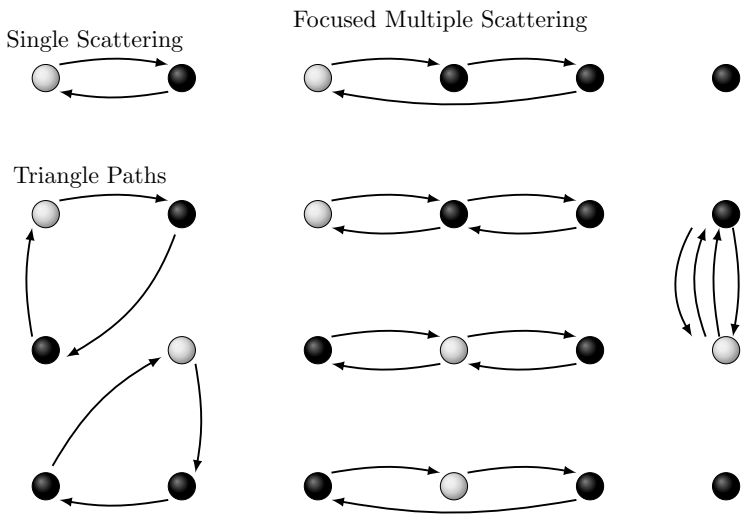

Figure 12. Multiple scattering paths for the photoelectron. While single-scattering paths generally dominate most EXAFS spectra, multiple scattering paths can give important contributions, especially in well-ordered crystalline materials. Fortunately, these terms can easily be included into the standard EXAFS formalism.

interatomic distances R sampled by an EXAFS measurement. As noted above, the core-hole lifetime is typically in the femtosecond range. Since thermal vibrations are on the picosecond time-scale, each X-ray absorbed in an EXAFS measurement gives a "snapshot" of the structure around 1 randomly selected absorbing atom in the sample, and the neighboring atoms will be essentially frozen in some configuration. Building up a full spectrum will result in a "blurry picture" due to the addition of many (often billions) of these snapshots. This has the important consequence that a single EXAFS measurement cannot distinguish thermal disorder due to atomic vibrations from static disorder.

An EXAFS measurement is then a *sampling* of the configuration of atoms around the average absorbing atom. Ignoring the contributions from multiple-scattering just discussed, the configuration of pairs of atoms is given by the Partial Pair Distribution function, $g(R)$, which gives the probability that an atom is found a distance R away from an atom of the selected type. Pair distribution functions are found from many structural probes (notably scattering techniques), but the Partial aspect is unique to EXAFS and other element-specific probes. EXAFS is sensitive only to the pairs of atoms that include the absorbing atom. Thus while scattering can give very accurate measures of the total pair distribution function, EXAFS is particularly useful for looking at low concentration elements in complex systems.

To better account for the sampling of $g(R)$ of any particular single-scattering shell of atoms, we should replace our σ^2 term with an integral over *all* absorbing atoms, as with (using a simplified form of the EXAFS Equation in exponential notation and recalling that k might be replaced by p, the complex wavenumber to account for the mean free path $\lambda(k)$):

$$\chi(k) = \left\langle \sum_j \frac{f_j(k) e^{i2kR_j + i\delta_j(k)}}{kR_j^2} \right\rangle$$

where the angle brackets mean averaging over the distribution function:

$$\langle x \rangle = \frac{\int dR\ x\ g(R)}{\int dR\ g(R)}$$

There are a few different approaches that can be used for modeling $g(R)$ in EXAFS. First, one can ask what the principal moments of $g(R)$ might be. Recognizing that e^{i2kR} term (or $\sin(2kR)$ term) is the most sensitive part to small changes in R, and pulling out the other terms, we have

$$\chi(k) = \sum_j f_j(k) \frac{e^{i\delta_j(k)}}{kR_j^2} \left\langle e^{i2kR_j} \right\rangle$$

This average of an exponential term can be described by the *cumulants* of the distribution $g(R)$, as

$$\left\langle e^{i2kR} \right\rangle = \exp\left[\sum_{n=1}^{\infty} \frac{(2ik)^n}{n!} C_n \right]$$

where the coefficients C_n are the cumulants. The cumulants of a distribution can be related to the more familiar moments of the distribution. The lowest order cumulants are

$$\begin{aligned}
C_1 &= \langle r \rangle \\
C_2 &= \langle r^2 \rangle - \langle r \rangle^2 \\
C_3 &= \langle r^3 \rangle - 3\langle r^2 \rangle \langle r \rangle + 2\langle r \rangle^3 \\
C_4 &= \langle r^4 \rangle - 3\langle r^2 \rangle^2 - 4\langle r^3 \rangle \langle r \rangle + 12\langle r^2 \rangle \langle r \rangle^2 - 6\langle r \rangle^4
\end{aligned}$$

where $r = R - R_0$ and R_0 is the mean R value of the distribution, and $\langle r^n \rangle$ is the n^{th} moment of the distribution. C_1 is then simply a shift in centroid, and C_2 is the mean-square-displacement, σ^2. C_3 and C_4 measure the skewness and kurtosis for the distribution, respectively, and are 0 for a Gaussian distribution. Because the low order terms in the cumulant expansion represent a small modification to the Gaussian approximation and can be readily applied to any spectrum, they are included in many analyses codes and discussed widely in the EXAFS literature. In particular, the skewness term, C_3, is sometimes found to be important in analysis of moderately disordered systems.

Another approach to modeling complex disorder is to parameterize $g(R)$ by some functional form and use this parameterization in the EXAFS Equation. This can be done either analytically by putting in a functional form for $g(R)$ (Filipponi et al. 1995), or by building a histogram with weights given by the parameterized $g(R)$. The latter approach can be readily done with many existing analysis tools, and can give noticeably better results than the cumulant expansion for very high disorder. For some problems, a more sophisticated analysis using a *Monte Carlo* approach of calculating the EXAFS for a large set of atomic clusters can be useful. For example, atomic configurations from a series of molecular dynamics simulations may be used to predict EXAFS spectra including complex configurations and disorder. Such work can be computationally intensive, but can also give additional insight into the interactions between atoms and molecules in complex systems. We'll continue to use N and σ^2 as the normal form of the EXAFS Equation, but will remember that these more complex descriptions of the distribution of atoms are possible and that we are not limited to studying well-behaved systems with Gaussian distributions.

Discussion

We've used a simple physical picture of photoelectron scattering to develop the EXAFS equation (Eqn. 10) that we can use in the quantitative analysis of EXAFS spectra. From Equation (10), we can draw a few physical conclusions about XAFS. First, because of the $\lambda(k)$ term and the R^{-2} term, XAFS is seen to be an inherently *local probe*, not able to see much further than 5 Å or so from the absorbing atom. Second, the XAFS oscillations consist of different frequencies that correspond to the different distances of atomic shells. This will lead us to use Fourier transforms in the analysis. Finally, in order to extract the distances and coordination numbers, we need to have accurate values for the scattering amplitude and phase-shifts $f(k)$ and $\delta(k)$ from the neighboring atoms.

This last point here—the need for accurate scattering amplitude and phase-shifts—has been a crucial issue in the field of EXAFS. Though early attempts to calculate the terms were qualitatively successful and instructive, they were generally not accurate enough to be used in analysis. In the earliest EXAFS analyses, these factors were most often determined from experimental spectra in which the near-neighbor distances and species were known. Such experimental standards can be quite accurate, but are generally restricted to first neighbor shell and to single-scattering. Since the 1990s, calculations of $f(k)$ and $\delta(k)$ have become more accurate and readily available, and use of experimental standards in EXAFS analysis is now somewhat rare, and restricted to studies of small changes in distances of fairly well-characterized systems. Calculated scattering factors are not without problems, but they have been shown numerous times to be accurate enough to be used in real analysis, and in some cases are more accurate than experimentally derived scattering factors. The calculated factors are not restricted to the first shell, and can easily account for multiple-scattering of the photoelectron. We'll use calculations of $f(k)$ and $\delta(k)$ from FEFF to model real data.

XAFS MEASUREMENTS: TRANSMISSION AND FLUORESCENCE

XAFS requires a very good measure of $\mu(E)$. Since the XAFS is a fairly small modulation of the total absorption, a fairly precise and accurate measurement of $\mu(E)$—typically to 10^{-3}—is required. Statistical errors in $\mu(E)$ due to insufficient count rates in intensities are rarely the limiting factor for most XAFS measurements, and can generally be overcome by counting longer. On the other hand, systematic errors in $\mu(E)$ can degrade or even destroy the XAFS, and are more difficult to eliminate. Fortunately, if care is taken in sample preparation, setting up the measurement system, and alignment of the sample in the beam, it is usually not too difficult to get good XAFS measurements.

A sketch of the basic experimental layout is given in Figure 13, showing a monochromatic beam of X-rays striking a sample and the intensities of the incident, transmitted, and emitted X-ray beams being measured. From this, it can be seen that the main experimental challenges are getting an X-ray source that can be reliably and precisely tuned to select a single X-ray energy, and 2) high-quality detectors of X-ray intensity. For most modern experiments, the X-ray source is a synchrotron radiation source, which provides a highly collimated beam of X-rays with a broad range of energies. A particular energy is selected with a double crystal monochromator, which consists of two parallel and nearly perfect crystals, typically silicon. The first crystal is centered in the incident X-ray beam from the source and rotated to a particular angle so as to reflect a particular energy by X-ray diffraction following Bragg's law. By using near-perfect crystals, the diffracted beam is very sharply defined in angle and so also has a very narrow energy range, and the reflectivity is near unity. The second crystal, with the same lattice spacing as the first, is rotated together with the first crystal, and positioned to intercept the diffracted beam and re-diffract so that it is parallel to the original X-ray beam, though typically offset vertically from it. Such a monochromator allows a wide energy range of monochromatic X-rays to be selected simply by rotating a single axis, and is widely used at synchrotron beamlines, and especially at beamlines designed for XAFS measurements.

The principle characteristics of a monochromator that are important for XAFS are *the energy resolution*, the reproducibility, and the stability of the monochromator. Energy resolutions of ≈ 1 eV at 10 keV are readily achieved with silicon monochromators using the Si(111) reflection, and are sufficient for most XAFS measurements. Higher resolution can be achieved by using a higher order reflection, such as Si(220) or Si(311), but this often comes at a significant loss of intensity. In addition, the angular spread of the incident X-ray beam from the source can contribute to the energy resolution, and many beamlines employ a reflective mirror that can be curved slightly to collimate the beam before the monochromator to improve resolution. While poor energy resolution can be detrimental to XAFS measurements, and

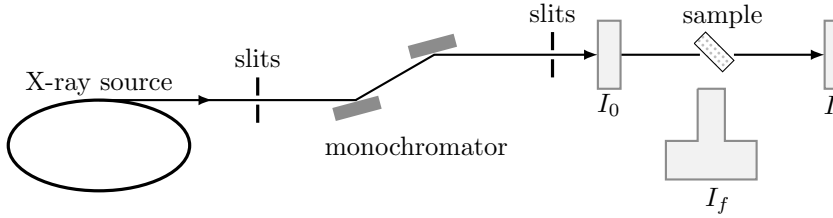

Figure 13. Sketch of an XAFS Experiment. An X-ray source, typically using synchrotron radiation, produces a collimated beam of X-rays with a broad energy spectrum. These X-rays are energy-selected by a slit and monochromator. The incident X-ray intensity, I_0, is sampled. XAFS can be recorded by measuring the intensity transmitted through the sample or by measuring the intensity of a secondary emission—typically X-ray fluorescence or Auger electrons resulting from the X-ray absorption. The X-ray energy is swept through and above the electron binding energy for a particular energy level of the element of interest.

especially for XANES measurements, most existing beamlines have resolution sufficient for good XAFS measurements.

Stability and reproducibility of monochromators is sometimes challenging, as the angular precisions of monochromators needed for XAFS are typically on the order of 10^{-4} degrees, so that a very small change in Bragg angle corresponds to a substantial energy shift. Very high quality rotation stages can essentially eliminate such drifts, but may not be installed at all beamlines. In addition, small temperature drifts of the monochromator can cause energy drifts, as the lattice constant of the crystal changes. Stabilizing the temperature of the monochromator is very important, but can be challenging as the power in the white X-ray beam from a modern synchrotron source can easily exceed 1 kW in a few square millimeters. For the most part, these issues are ones of beamline and monochromator design and operation, generally solved by the beamline, and are not a significant problem at modern beamlines designed for XAFS measurements. Still, these issues are worth keeping in mind when assessing XAFS data.

Despite their name, monochromators based on Bragg diffraction do not select only one energy (or color) of light, but also certain *harmonics* (integer multiples) of that energy. While these higher energies will be far above the absorption edge, and so not be absorbed efficiently by the sample, they can cause subtle problems with the data that can be hard to diagnose or correct afterward. These include sharp changes or *glitches* in intensity at particular energies, and unexpectedly large noise in the data. There are two main strategies for removing harmonics. The first is to slightly misalign or "de-tune" the two crystals of the monochromator. This will reduce the transmitted intensity of the higher-energy harmonics much more than it reduces the intensity of the fundamental beam. De-tuning in this way can be done dynamically, often by putting a small piezo-electric crystal on the second monochromator crystal to allow fine motions to slightly misalign the two crystals. The second method for removing harmonics is to put a reflective X-ray mirror in the beam so that it reflects the fundamental beam but not the higher energy harmonics. Such a harmonic-rejection mirror is generally more efficient at removing the higher harmonics than de-tuning the monochromator crystals. Ideally, both of these strategies can be used, but it is generally necessary to use at least one of these methods.

Having linear detectors to measure I_0 and I for transmission measurements is important for good XAFS measurements, and not especially difficult. A simple ion chamber (a parallel plate capacitor filled with an inert gas such nitrogen or argon, and with a high voltage across it through which the X-ray beam passes) is generally more than adequate, as these detectors themselves are generally very linear over a wide range of X-ray intensities. The currents generated from the detectors are quite low (often in the picoampere range, and rarely above a few microampere) and so need to be amplified and transmitted to a counting system. Noise in transmission lines and linearity of the amplification systems used for ion chambers (and other detectors) can cause signal degradation, so keeping cables short and well-grounded is important. Typical current amplifiers can have substantial non-linearities at the low and high ends of their amplification range, and so have a range of linearity limited to a few decades. For this reason, significant dark currents are often set and one must be careful to check for saturation of the amplifiers. In addition, one should ensure that the voltage applied across the ion chamber plates is sufficiently high so that all the current is collected—simply turning up the voltage until the intensity measured for an incident beam of constant intensity is itself constant and independent of voltage is generally sufficient. Such checks for detector linearity can be particularly important if glitches are detected in a spectrum. For fluorescence measurements, several kinds of detectors can be used in addition to ion chambers, and linearity can become an important issue and depend on details of the detector.

With a good source of monochromatic X-rays and a good detection system, accurate and precise transmission measurements on uniform samples of appropriate thickness, are generally easy. Some care is required to make sure the beam is well-aligned on the sample and that

harmonics are not contaminating the beam, but obtaining a noise level of 10^{-3} of the signal is generally easy for transmission measurements. Such a noise level is achievable for fluorescence measurements but can be somewhat more challenging, especially for very low concentration samples.

Transmission XAFS measurements

For concentrated samples, in which the element of interest is a major component—10% by weight or higher is a good rule of thumb—XAFS should be measured in transmission. To do this, one needs enough transmission through the sample to get a substantial signal for I. With $\mu t = \ln(I/I_0)$, we typically adjust the sample thickness t so that $\mu t \approx 2.5$ above the absorption edge and/or the edge step $\Delta\mu(E)t \approx 1$. For Fe metal, this gives $t = 7$ μm, while for many solid metal-oxides and pure mineral phases, t is typically in the range of 10 to 25 μm. For concentrated solutions, sample thickness may be several millimeter thick, but this can vary substantially. If both $\mu t \approx 2.5$ for the total absorption and an edge step $\Delta\mu(E)t \approx 1$ cannot be achieved, it is generally better to have a smaller edge step, and to keep the total absorption below $\mu t \approx 4$, so that enough X-rays are transmitted through the sample to measure. Tabulated values for $\mu(E)$ for the elements are widely available, and software such as HEPHAESTUS (Ravel and Newville 2005) can assist in these calculations.

In addition to being the appropriate thickness for transmission measurements, the sample must be of uniform thickness and free of pinholes. Non-uniformity (that is, variations in thickness of 50% or so) and pinholes in the sample can be quite damaging, as μ is logarithmic in I. Since the portion of the beam going through a small hole in the sample will transmit with very high intensity, it will disproportionately contribute to I compared to the parts of the beam that actually goes through the sample. For powdered material, the grain size cannot be much bigger than an absorption length, or the thickness variation across the particle will lead to non-linear variations in the beam transmitted through the sample. If these challenging conditions can be met, a transmission measurement is very easy to perform and gives excellent data. This method is usually appropriate for pure mineral and chemical phases, or for other systems in which the absorbing element has a concentrations > 10%.

A few standard methods for making uniform samples for transmission XAFS exist. If one can use a solution or has a thin, single slab of the pure material (say, a metal foil, or a sample grown in a vacuum chamber), these can make ideal samples. For many cases, however, a powder of a reagent grade chemical or mineral phase is the starting material. Because the required total thickness is so small, and uniformity is important, grinding and sifting the powder to select the finest grains can be very helpful. Using a solvent or other material in the grinding process can be useful. In some case, suspending a powder in a solvent to skim off the smallest particles held up by surface tension can also be used. Spreading or painting the grains onto sticky tape and shaking off any particles that don't stick can also be used to select the finest particles, and can make a fairly uniform sample, with the appropriate thickness built up by stacking multiple layers. Ideally, several of these techniques can be used in combination.

Fluorescence and electron yield XAFS measurements

For samples that cannot be made thin enough for transmission or with the element of interest at lower concentrations (down to a few ppm level in some cases), monitoring the X-ray fluorescence is the preferred technique for measuring the XAFS. In a fluorescence XAFS measurement, the X-rays emitted from the sample will include the fluorescence line of interest, fluorescence lines from other elements in the sample, and both elastically and inelastically (Compton) scattered X-rays. An example fluorescence spectrum is shown in Figure 14. This shows Fe K_α and K_β fluorescence lines along with the elastically scattered peak (unresolvable from the Compton scatter), as well as fluorescence lines from Ca, Ti, and V. In many cases the scatter or fluorescence lines from other elements will dominate the fluorescence spectrum.

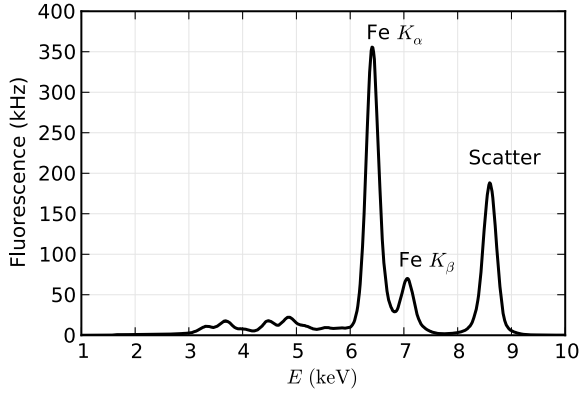

Figure 14. X-ray fluorescence spectrum from an Fe-rich mineral (a feldspar), showing the Fe K_α and K_β emission lines around 6.4 and 7.0 keV, and the elastically (and nearly-elastically) scattered peak near 8.5 keV. At lower energies, peaks for Ca, Ti, and V can be seen.

There are two main considerations for making good fluorescence XAFS measurements: the solid angle collected by the detector, and the energy resolution of the detector for distinguishing the fluorescence lines. The need for solid angle is easy to understand. The fluorescence is emitted isotropically, and we'd like to collect as much of the available signal as possible. X-rays that are elastically and inelastically scattered (for example, by the Compton scattering process) by the sample are not emitted isotropically because the X-rays from a synchrotron are *polarized* in the plane of the synchrotron, (a fact we've neglected up to this point). This polarization means that elastic scatter is greatly suppressed at 90° to the incident beam, in the horizontal plane. Therefore, fluorescence detectors are normally placed perpendicular to the incident beam, and in the horizontal plane.

Energy resolution for a fluorescence detector can be important as it allows discrimination of signals based on energy, so that scattered X-rays and fluorescence lines from other elements can be suppressed relative to the intensity of the fluorescence lines of interest. This lowers the background intensity, and increases the signal-to-noise level. Energy discrimination can be accomplished either physically, by filtering out unwanted emission before it gets to the detector, or electronically after it is detected, or both.

An example of a commonly used physical filter is to place a Mn-rich material between an Fe-bearing sample and the fluorescence detector. Due to the Mn K absorption edge, the filter will preferentially absorb the elastic and inelastic scatter peak and pass the Fe K_α line, as shown in Figure 15. For most K edges, the element with $Z-1$ of the element of interest can be used to make an appropriate filter, and suitable filters can be found for most of the L-edges. A simple filter like this can be used with a detector without any intrinsic energy resolution, such as an ion chamber or large PIN diode. To avoid re-radiation from the filter itself, Soller slits, as shown in Figure 16, can be used to preferentially collect emission from the sample and block most of the signal generated away from the sample from getting into the fluorescence detector, including emission from the filter itself. Such an arrangement can be very effective especially when the signal is dominated by scatter, as when the concentration of the element of interest is in the range of hundreds of ppm or lower, and the matrix is dominated by light elements, with few other heavy elements that have fluorescence lines excited by the incident beam.

Energy discrimination can also be done electronically on the measured X-ray emission spectrum after it has been collected in the detector. A common example of this approach uses a solid-state Si or Ge detector, which can achieve energy resolution of ≈ 200 eV or better

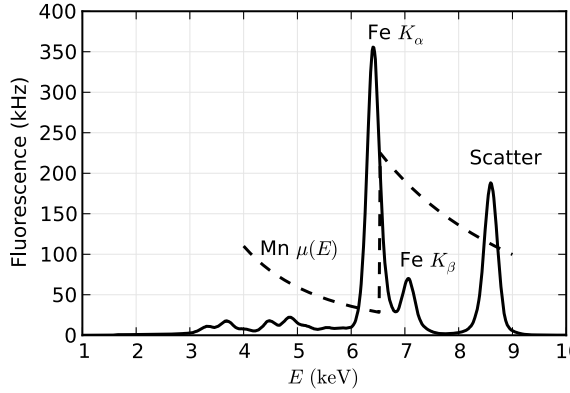

Figure 15. The effect of a "Z−1" filter on a measured fluorescence spectrum. A filter containing Mn placed between sample and detector will absorb most of the scatter peak, while transmitting most of the Fe K_α emission. For samples dominated by the scatter peak, such a filter can dramatically improve the signal-to-noise level.

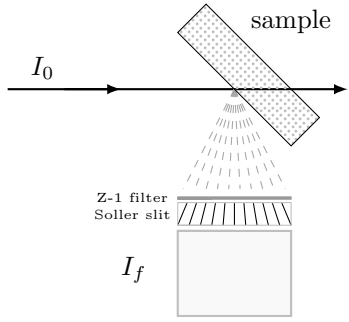

Figure 16. The practical use of "Z−1" filter for energy discrimination of a fluorescence spectrum. The filter placed between sample and detector will absorb most of the scatter peak. Because the filter can itself re-radiate, a set of metal Soller slits pointing at the sample will preferentially absorb the emission from the filter and prevent it from entering the detector.

(approaching 130 eV for modern silicon detectors). The spectrum shown in Figure 14 was collected with such a Ge solid-state detector. These detectors have an impressive advantage of being able to measure the full X-ray fluorescence spectrum, which is useful in its own right for being able to identify and quantify the concentrations of other elements in the sample. Because unwanted portions of the fluorescence spectrum can be completely rejected electronically, these detectors can have excellent signal-to-background ratios and be used for XAFS measurements with concentrations down to ppm levels. Though solid-state detectors have many advantages, they have a few drawbacks:

1. The electronic energy discrimination takes a finite amount of time, which limits the total amount of signal that can be processed. These detectors typically saturate at $\approx 10^5$ Hz of *total* count rate or so. When these rates are exceeded, the detector is effectively unable to count all the fluorescence, and is said to be "dead" for some fraction of the time. It is common to use ten or more such detectors in parallel. Even then, the limit on total intensity incident for these detectors can limit the quality of the measured XAFS.

2. Maintaining, setting up, and using one of these is much more work than using an ion chamber. For example, germanium solid-state detectors must be kept at liquid nitrogen temperatures. The electronics needed for energy discrimination can be complicated, expensive, and delicate.

Despite these drawbacks, the use of solid-state detectors is now fairly common practice for XAFS, especially for dilute and heterogeneous samples, and the detectors and electronics themselves are continually being improved.

Before we leave this section, there are two import effects to discuss for XAFS measurements made in fluorescence mode. These are *self-absorption* or *over-absorption* from the sample, and a more detailed explanation of deadtime effects for measurements made with solid-state detectors. If not dealt with properly, these effects can substantially comprise otherwise good fluorescence XAFS data, and so it is worth some attention to understand these in more detail.

Self-absorption (or over-absorption) of fluorescence XAFS

The term *self-absorption,* when referred to fluorescence XAFS, can be somewhat confusing. Certainly, the sample itself can absorb many of the fluoresced X-rays. For example, for a dilute element (say, Ca) in a relatively dense matrix (say, iron oxide), the Ca fluorescence will be severely attenuated by the sample and the measured fluorescence signal for Ca will be dictated by the escape depth of the emitted X-ray in the matrix. Although this type of absorbtion is an important consideration, this is not what is usually meant by the term *self-absorption* in EXAFS. Rather, the term self-absorption for EXAFS usually refers to the situation in which the penetration depth into the sample is dominated by the element of interest, and so is one special case of the term as used in X-ray fluorescence analysis. In the worst case for self-absorption (a very thick sample of a pure element), the XAFS simply changes the penetration depth into the sample, but essentially all the X-rays are absorbed by the element of interest. The escape depth for the fluoresced X-ray is generally much longer than the penetration depth (as the fluoresced X-ray is below the edge energy), so that most absorbed X-rays will generate a fluoresced X-ray that will escape from the sample. This severely dampens the XAFS oscillations, and for a very concentrated sample, there may be no XAFS oscillations at all. With this understanding of the effect, the term *over-absorption* (Manceau et al. 2002) is probably a better description, and should be preferred to *self-absorption* even though the latter is in more common usage.

Earlier we said that for XAFS measured in fluorescence goes as

$$\mu(E) \propto \frac{I_f}{I_0}$$

This is a slight oversimplification. The probability of fluorescence is proportional to the absorption probability but the fluorescence intensity that we measure has to travel back through the sample to get to the detector. Since all matter attenuates X-rays, the fluorescence intensity, and therefore the XAFS oscillations, can be damped. More correctly, the measured fluorescence intensity goes as (see Fig. 17)

$$I_f = I_0 \frac{\varepsilon \Delta\Omega}{4\pi} \frac{\mu_\chi(E)\left\{1 - e^{-\left[\frac{\mu_{tot}(E)}{\sin\theta} + \frac{\mu_{tot}(E_f)}{\sin\phi}\right]t}\right\}}{\frac{\mu_{tot}(E)}{\sin\theta} + \frac{\mu_{tot}(E_f)}{\sin\phi}} \tag{11}$$

where ε is the fluorescence efficiency, $\Delta\Omega$ is the solid angle of the detector, E_f is the energy of the fluorescence X-ray, θ is the incident angle (between incident X-ray and sample surface), ϕ is the exit angle (between fluoresced X-ray and sample surface), $\mu_\chi(E)$ is the absorption from the element of interest, and $\mu_{tot}(E)$ is the *total* absorption in the sample,

$$\mu_{tot}(E) = \mu_\chi(E) + \mu_{other}(E)$$

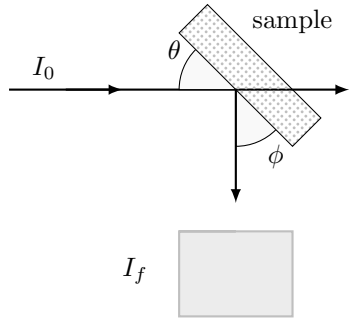

Figure 17. Fluorescence XAFS measurements, showing incident angle θ and exit angle φ.

and $\mu_{other}(E)$ is the absorption due to lower energy edges of the element of interest and other elements in the sample. Equation (11) has several interesting limits that are common for real XAFS measurements. First, there is the thin sample limit, in which $\mu_{tot}t << 1$. The $1 - e^{-\mu t}$ term then becomes (by a Taylor series expansion)

$$1 - e^{-\mu t} \approx \left[\frac{\mu_{tot}(E)}{\sin\theta} + \frac{\mu_{tot}(E_f)}{\sin\phi} \right] t$$

which cancels the denominator, so that

$$I_f \approx I_0 \frac{\varepsilon \Delta\Omega}{4\pi} \mu_\chi(E) t$$

Alternatively, there is the *thick, dilute sample limit*, for which $\mu t >> 1$ and $\mu_\chi << \mu_{other}$. Now the exponential term goes to 0, so that

$$I_f = I_0 \frac{\varepsilon \Delta\Omega}{4\pi} \frac{\mu_\chi(E)}{\frac{\mu_{tot}(E)}{\sin\theta} + \frac{\mu_{tot}(E_f)}{\sin\phi}}$$

In this case we can also ignore the energy dependence of μ_{tot}, leaving

$$I_f \propto I_0 \mu_\chi(E)$$

These two limits (very thin or thick, dilute samples) are the best cases for fluorescence measurements.

For relatively thick and concentrated samples, for which $\mu_\chi \approx \mu_{other}$, we cannot ignore the energy dependence of μ_{tot}, and must correct for the oscillations in $\mu_{tot}(E)$ in Equation (11). As said above, for very concentrated samples, $\mu_{tot}(E) \approx \mu_\chi(E)$, and the XAFS can be completely lost. On the other hand, if the self-absorption is not too severe, it can be corrected using the above equations (Pfalzer et al. 1999; Booth and Bridges 2005).

Finally, these self-absorption effects can be reduced for thick, concentrated samples by rotating the sample so that it is nearly normal to the incident beam. With $\phi \rightarrow 0$ or the *grazing exit limit*, $\mu_{tot}(E_f)/\sin\phi >> \mu_{tot}(E)/\sin\theta$, which gives

$$I_f \approx I_0 \frac{\varepsilon \Delta\Omega}{4\pi} \frac{\mu_\chi(E)}{\mu_{tot}(E_f)/\sin\phi}$$

and gets rid of the energy dependence of the denominator.

In certain situations, monitoring the intensity of emitted electrons (which includes both Auger electrons and lower-energy secondary electrons) can be used to measure the XAFS. The escape depth for electrons from materials is generally much less than a micron, making these measurements more surface-sensitive than X-ray fluorescence measurements, and essentially immune to over-absorption. Because the relative probability for emitting an electron instead of an X-ray is higher for low energy edges and electron levels, electron yield measurements are much more common and efficient for lower energy edges. Electron yield measurements are generally most appropriate for samples that are metallic or semiconducting (that is, electrically conducting enough so that the emitted electrons can be replenished from a connection to ground, without the sample becoming charged). In order to collect the electron yield signal, a voltage-biased collector needs to be placed very close to the sample surface, typically with a helium atmosphere or vacuum between sample and collector. While electron yield measurements can give very good data, for the reasons mentioned here, measuring XAFS in electron yield is not very common for X-ray energies above 5 keV, and further details of these measurements will be left for further reading.

Deadtime corrections for fluorescence XAFS

For fluorescence XAFS data measured with an energy discriminating fluorescence detector, such as a solid-state Ge or Si detector, it is often necessary to correct for the so-called *deadtime effect*. This accounts for the fact that a finite amount of time is needed to measure the energy of each X-ray detected, and the electronics used to make this measurement can only process one X-ray at a time. At high enough incident count rates, the detector electronics cannot process any more counts and is said to be *saturated*. The incident count rate is due to all the X-rays in the detector, not just from the fluorescence line used in the XAFS measurements. Saturation effects are particularly important when the absorbing atom is of relatively high concentration (above a few percent by weight), because the intensity of the monitored fluorescence line is negligible below the edge, and grows dramatically at the absorption edge. Such an increase in intensity can cause a non-linear reduction of the fluorescence intensity, giving a non-linear artifact to the XAFS.

Fortunately, most energy discriminating detector and electronics systems can be characterized with a simple parameter τ that relates the incident count rate with the output count rate actually processed as

$$I_{\mathrm{out}} = I_{\mathrm{inp}} e^{-I_{\mathrm{inp}}\tau}$$

where I_{inp} is the incident count rate to the detector, I_{out} is the output count rate, giving the intensity reported by the detector, and τ is the deadtime, characteristic of the detector and electronics system. For a realistic value of $\tau = 2$ μs, the relation of input count rate and output count rate is shown in Figure 18. For many detector systems, there is some ability to adjust τ and the maximum output count rate, that can be achieved, but at the expense of energy resolution of the fluorescence spectra. In order to make this correction, one wants to get I_{inp} given I_{out} which can be complicated near the saturation value for I_{inp}, as a particular value recorded for I_{out} could come from one of two values for I_{inp}. For some detector systems, one can simply record I_{inp} and I_{out} for each measurement as an output of the detector and electronics system. Alternatively, one can separately measure τ so that the corrections can be applied easily. Otherwise, a good rule of thumb is that spectra can be corrected up to a rate for which I_{out} is half of I_{inp} (I_{inp} around 350 kHz for the curve shown in Fig. 18). Importantly, for multi-element detector systems, each detector element will have its own deadtime, and corrections should be made for each detector before summing the signals from multiple detectors.

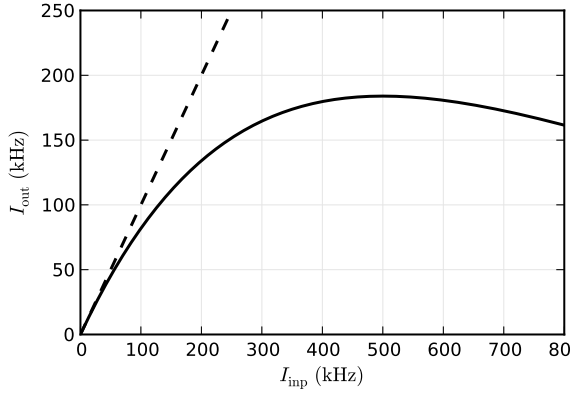

Figure 18. Typical deadtime curve for a pulse-counting, energy-discriminating detector with a deadtime τ of 2 μs. At low input count rates, the output count rate—the rate of successfully processed data—rises linearly. As the count rate increases, some of the pulses cannot be processed, so that the output count rate is lower than the input count rate. At *saturation*, the output count rate cannot go any higher, and increasing the input count rate will decrease the output rate. The dashed line shows a line with unity slope, for a detector with no deadtime.

XAFS DATA REDUCTION

For all XAFS data, whether measured in transmission or fluorescence (or electron emission), the data reduction and analysis are essentially the same. First, the measured intensity signals are converted to $\mu(E)$, and then reduced to $\chi(k)$. After this data reduction, $\chi(k)$ can be analyzed and modeled using the XAFS equation. In this section, we'll go through the steps of data reduction, from measured intensities to $\chi(k)$, which generally proceeds as:

1. Convert measured intensities to $\mu(E)$, possibly correcting systematic measurement errors such as self-absorption effects and detector deadtime.
2. Identify the threshold energy E_0, typically as the energy of the maximum derivative of $\mu(E)$.
3. Subtract a smooth pre-edge function from $\mu(E)$ to get rid of any instrumental background and absorption from other edges.
4. Determine the edge jump, $\Delta\mu$, at the threshold energy, and normalize $\mu(E)$, so that the pre-edge subtracted and normalized $\mu(E)$ goes from approximately 0 below the threshold energy to 1 well above the threshold energy. This represents the absorption of a single X-ray, and is useful for XANES analysis.
5. Remove a smooth post-edge background function approximating $\mu_0(E)$, thereby isolating the XAFS $\chi = (\mu - \mu_0)/\Delta\mu$.
6. Convert χ from energy E to photoelectron wavenumber $k = \sqrt{2m(E - E_0)/\hbar^2}$.
7. k-weight the XAFS $\chi(k)$ and Fourier transform into R-space.

We'll go through each of these steps in slightly more detail, and show them graphically using real XAFS data.

As with many things, the first step is often the most challenging. Here, the differences between measurements made in transmission and fluorescence mode are most pronounced. For transmission measurements, we rearrange Equation (1), and ignore the sample thickness, so that

$$\mu(E) = \ln\left(\frac{I_0}{I}\right)$$

where now I_0 and I are the signals measured from the ion chambers. Typically, the signals measured as I_0 and I are actually integrated voltages over some predefined time where the voltages are taken from the output of current amplifiers with input currents from ion chambers as input. Thus the measurements are not the incident flux in photons per second. Rather, they are scaled measures of the flux *absorbed* in the ion chamber. For the most part, the difference between what we think of as I_0 (incident X-ray flux, in photons/second) and what we actually measure for I_0 (scaled, integrated current generated from X-rays absorbed in the ion chamber) is not very significant. When we take the ratio between the two ion chamber signals most of the factors that distinguish the conceptual intensity from the measured signal will either cancel out, give an arbitrary offset, or give a slowly varying monotonic drift with energy. Thus, it is common to see experimental values reported for "raw" $\mu(E)$ in the literature that do not have dimensions of inverse length, and which might even have values that are negative. For real values of $\mu(E)$ in inverse length, these measurements would be nonsensical, but for XAFS work this is of no importance, as we'll subtract off a slowly varying background anyway.

For fluorescence or Auger measurements, the situation is similar, except that one uses

$$\mu(E) = \frac{I_f}{I}$$

where I_f is the integrated fluorescence signal of interest. As with the transmission measurements, there is generally no need to worry about getting absolute intensities, and one can simply use the ratio of measured intensities. Because the instrumental drifts for a solid-state, energy-discriminating fluorescence detector may be different than for a gas-filled ion chamber, it is not unusual for $\mu(E)$ for fluorescence XAFS measurements to have an overall upward drift with energy, where transmission XAFS tends to drift down with energy.

In addition to the corrections for over-absorption and deadtime effects discussed in the previous section, other corrections may need to be made to the measured $\mu(E)$ data. For example, sometimes bad glitches appear in the data that are not normalized away by dividing by I_0. This is often an indication of insufficient voltage in ion chambers, of too much harmonic content in the X-ray beam, poorly uniform samples, incomplete deadtime correction, or a combination of these. If possible, it is preferred to address these problems during the measurement, but this is not always possible. For such glitches, the best approach is simply to remove them from the data—asserting that they were not valid measurements of $\mu(E)$.

Another example of a correction that can be made in the data reduction step is for cases where another absorption edge occurs in the spectrum. This could be from the same element (as is over the case for measurements made at the L_{III} edge, where the L_{II} edge will eventually be excited, or from a different element in a complex sample. As with a glitch, the appearance of another edge means that $\mu(E)$ is no longer from the edge and element of interest, and it is best to simply truncate the data at the other edge.

Pre-edge subtraction and normalization

Once the measurement is converted to $\mu(E)$, the next step is usually to identify the edge energy. Since XANES features can easily move the edge by several eV, and because calibrations vary between monochromators and beamlines, it is helpful to be able to do this in an automated way that is independent of the spectra. Though clearly a crude approximation, the most common approach is to take the maximum of the first derivative of $\mu(E)$. Though it has little theoretical justification, it is easily reproduced, and so can readily be checked and verified.

Instrumental drifts from detector systems can be crudely approximated by a simple linear dependence in energy. That is, a linear fit to the pre-edge range of the measured spectrum is found, and subtracted. In some cases, a so-called Victoreen pre-edge function (in which one fits a line to $E^n\mu(E)$ for some value of n, typically 1, 2 or 3) can do a slightly better job at approximating the instrumental drifts for most XAFS spectra. This is especially useful for dilute data measured in fluorescence with a solid-state detector, where the contribution from elastic and Compton-scattered intensity into the energy window of the peak of interest will decrease substantially with energy, as the elastic peak moves up in energy.

The next step in the process is to adjust the scale of $\mu(E)$ to account for the absorption of 1 photoelectron. By convention, we *normalize* the spectrum to go from approximately 0 below the edge to approximately 1 above the edge. To do this, we find the edge step, $\Delta\mu$, and divide $\mu(E)$ by this value. Typically, a low-order polynomial is fitted to $\mu(E)$ well above the edge (away from the XANES region), and the value of this polynomial is extrapolated to E_0 to give the edge step. It should be emphasized that this convention is fairly crude and can introduce systematic biases in the result for $\Delta\mu$.

Examples of these processing steps (location of E_0, subtraction of pre-edge, and normalization to an edge jump of 1) for transmission XAFS data at the Fe *K*-edge of FeO are shown in Figures 19 and 20. For XANES analysis, this amount of data reduction is generally all that is needed. For both XANES and EXAFS analysis, the most important part of these steps is the normalization to the edge step. For XANES analysis, spectra are generally compared by amplitude, so an error in the edge step for any spectra will directly affect the weight given to that spectra. For EXAFS, the edge step is used to scale $\chi(k)$, and so is directly proportional to coordination number. Errors in the edge step will translate directly to errors in coordination number. Getting good normalization (such that $\mu(E)$ goes to 1 above the edge) is generally not hard, but requires some care, and it is important to assess how well and how consistently this normalization process actually works for a particular data set. Most existing analysis packages do these steps reasonably well, especially in making spectra be normalized consistently, but it is not at all unusual for such automated, initial estimates of the edge step to need an adjustment of 10%.

Background subtraction

Perhaps the most confusing and error-prone step in XAFS data reduction is the determination and removal of the post-edge background function that approximates $\mu_0(E)$. This is

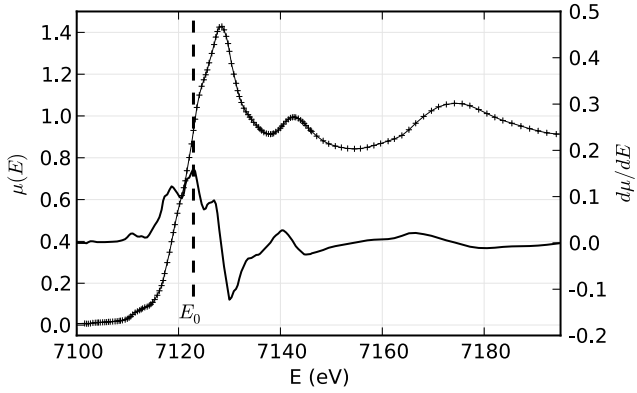

Figure 19. The XANES portion of the XAFS spectrum (solid with +), and the identification of E_0 from the maximum of the derivative $d\mu/dE$ (solid). This selection of E_0 is easily reproduced but somewhat arbitrary, so we may need to refine this value later in the analysis.

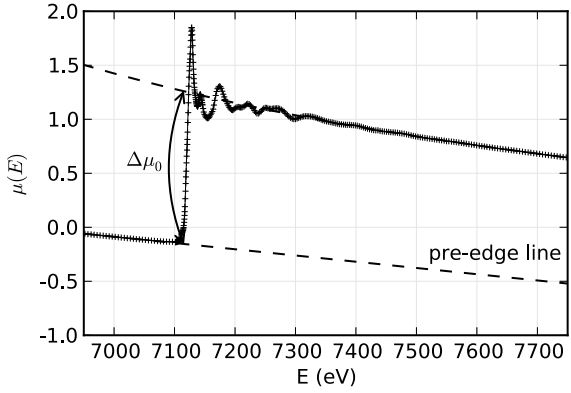

Figure 20. XAFS pre-edge subtraction and normalization. A line (or simple, low-order polynomial) is fit to the spectrum below the edge, and a separate low-order polynomial is fit to the spectrum well above the edge. The edge jump, $\Delta\mu_0$, is approximated as the difference between these two curves at E_0. Subtracting the pre-edge polynomial from the full spectrum and dividing by the edge jump gives a normalized spectrum.

somewhat unfortunate, as it does not need to be especially difficult. Since $\mu_0(E)$ represents the absorption coefficient from the absorbing atom without the presence of the neighboring atoms, we cannot actually measure this function separately from the EXAFS. In fact, even if possible, measuring $\mu(E)$ for an element in the gas phases would not really be correct, as $\mu_0(E)$ represents the absorbing atom embedded in the molecular or solid environment, just without the scattering from the core electrons of the neighboring atoms. Instead of even trying to measure an idealized $\mu_0(E)$, we determine it empirically by fitting a *spline* function to $\mu(E)$. A spline is a piece-polynomial function that is designed to be adjustable enough to smoothly approximate an arbitrary waveform, while maintaining convenient mathematical properties such as continuous first and second derivatives. This is certainly an *ad hoc* approach, without any real physical justification. Still, it is widely used for EXAFS analysis, and has the advantage of being able to account for those systematic drifts in our measurement of $\mu(E)$ that make it differ from the true $\mu(E)$, as long as those drifts vary slowly with energy. The main challenge with using an arbitrary mathematical spline to approximate $\mu_0(E)$ is to decide how flexible to allow it to be, so as to ensure that it does not follow $\mu(E)$ closely enough to remove the EXAFS. That is, we want $\mu_0(E)$ to remove the slowly varying parts of $\mu(E)$ while not changing $\chi(k)$, the part of $\mu(E)$ that varies more quickly with E.

A simple approach for determining $\mu_0(E)$ that works well for most cases relies on the Fourier transform to mathematically express the idea that $\mu_0(E)$ should match the slowly varying parts of $\mu(E)$ while leaving the more quickly varying parts of $\mu(E)$ to give the EXAFS χ. The Fourier transform is critical to EXAFS analysis, and we'll discuss it in more detail shortly, but for now the most important thing to know is that it gives a weight for each frequency making up a waveform. For EXAFS, the Fourier transform converts χ from wavenumber k to distance R.

For determining the background $\mu_0(E)$, we want a smoothly varying spline function that removes the low-R components of χ, while retaining the high-R components. Conveniently, we have a physically meaningful measure of what distinguishes "low-R" from "high-R," in that we can usually guess the distance to the nearest neighboring atom, and therefore assert that there should be no signal in the EXAFS originating from atoms at shorter R. As a realistic rule of thumb, it is rare for atoms to be closer together than about 1.5 Å—this is especially true for the heavier elements for which EXAFS is usually applied. Thus, we can assert that a

spline should be chosen for $\mu_0(E)$ that makes the resulting χ have as little weight as possible below some distance R_{bkg}, while ignoring the higher R components of χ. This approach and the use of R_{bkg}, with a typical value around 1 Å, as the cutoff value for R (Newville et al. 1993), is not always perfect, but can be applied easily to any spectra to give a spline function that reasonably approximates $\mu_0(E)$ for most spectra with at least some physically meaningful basis. Figure 21 shows a typical background spline found for FeO, using a high-R cutoff R_{bkg} of 1.0 Å. The resulting $\chi(k)$ is shown in Figure 22.

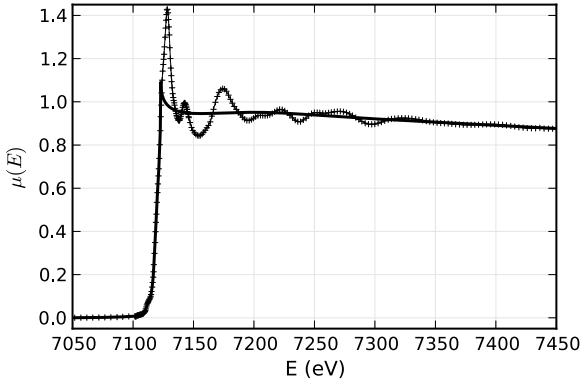

Figure 21. Post-edge background subtraction of FeO EXAFS. The background $\mu_0(E)$ is a smooth spline function that matches the low-R components of $\mu(E)$, in this case using 1 Å for R_{bkg}.

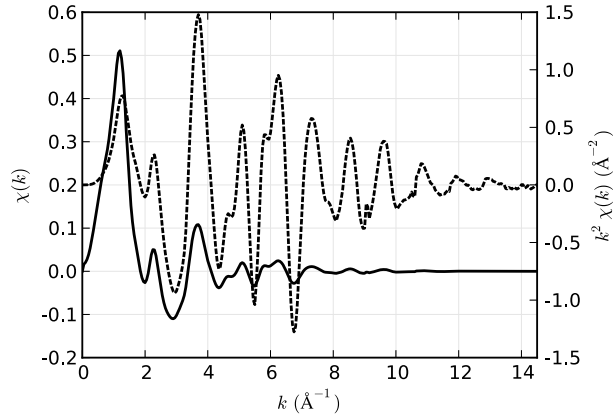

Figure 22. The EXAFS $\chi(k)$ (solid) isolated after background subtraction. The EXAFS decays quickly with k, and weighting by (dashed) amplifies the oscillations at high k.

The effect of varying R_{bkg} on the resulting spline for $\mu_0(E)$ and χ in both k- and R-space can be seen in Figure 23. Here, $\mu_0(E)$ spectra are shown for the same FeO $\mu(E)$ using values for R_{bkg} of 0.2, 1.0, and 4.0 Å. A value for R_{bkg} that is too small (shown with a solid line) results in $\mu_0(E)$ that does not vary enough, giving a slow oscillation in $\chi(k)$, and spurious peak below 0.5 Å in $|\chi(R)|$. On the other hand, setting R_{bkg} too high (shown with a dashed line) may result in a $\mu_0(E)$ that matches all the EXAFS oscillations of interest. Indeed, with R_{bkg} = 4 Å, both the first and second shells of the FeO EXAFS are entirely removed, leaving only the highest R components. This is clearly undesirable. In general, it is not too difficult to find a suitable value for R_{bkg}, with 1 Å or half the near-neighbor distance being fine default choices. As we can see from Figure 23, having R_{bkg} too small is not always a significant problem—the low R peak can simply be ignored in the modeling of the spectra, and there is little effect on the spectrum at higher R.

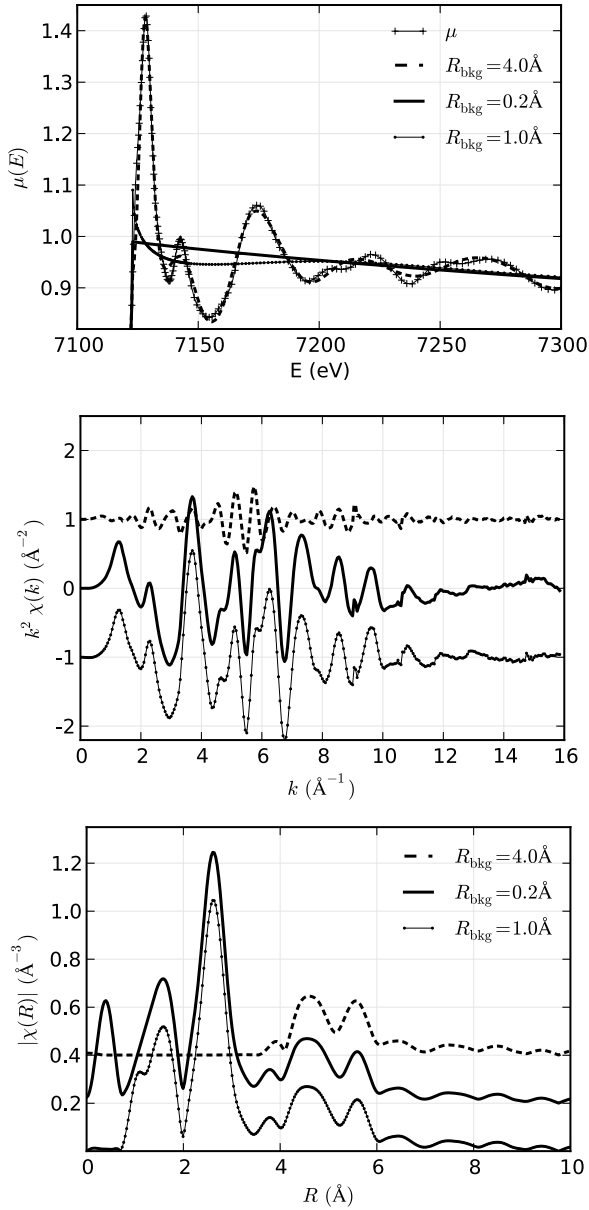

Figure 23. The effect of changing R_{bkg} on $\mu_0(E)$ and χ. A typical value for R_{bkg} of 1.0 Å (dots) results in a spline for (E) that can follow the low-R variations in $\mu(E)$ while not removing the EXAFS. A value too small (R_{bkg} = 0.2 Å, solid) gives a spline that is not flexible enough, leaving a low-R artifact, but one that will not greatly impact further analysis. On the other hand, too large a value (R_{bkg} = 4.0 Å, dashed) will give a spline flexible enough to completely remove the first and second shells of the EXAFS.

EXAFS Fourier transforms

As mentioned above, the Fourier transform is central for the understanding and modeling of EXAFS data. Indeed, the initial understanding of the phenomena was aided greatly by the

ability to perform Fourier transforms on measured EXAFS spectra. While there are certainly ample resources describing Fourier transforms and their properties, a few important points about the use of Fourier transforms for EXAFS will be made here.

The first thing to notice from Figure 24 is that two peaks are clearly visible—these correspond to the Fe-O and Fe-Fe distances in FeO. Thus the Fourier transformed XAFS can be used to isolate and identify different coordination spheres around the absorbing Fe atom. Indeed, $|\chi(R)|$ almost looks like a radial distribution function, $g(R)$. While EXAFS does depend on the partial pair distribution—the probability of finding an atom at a distance R from an atom of the absorbing species—$\chi(R)$ is certainly not just a pair distribution function. This can be seen from the additional parts to the EXAFS Equation, including the non-smooth k dependence of the scattering factor $f(k)$ and phase-shift $\delta(k)$.

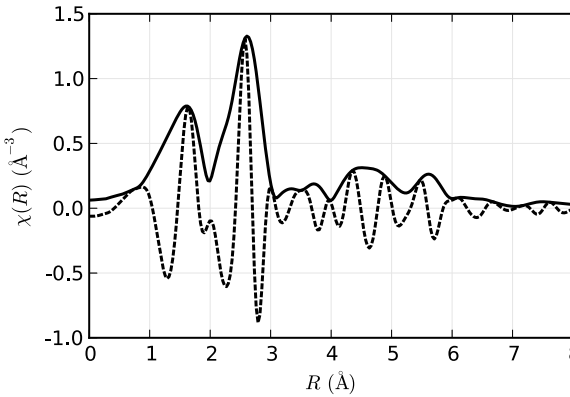

Figure 24. The Fourier Transformed XAFS, $\chi(R)$. The magnitude $|\chi(R)|$ (solid) is the most common way to view the data, but the Fourier transform makes $\chi(R)$ a complex function, with both a real (dashed) and imaginary part, and the magnitude hides the important oscillations in the complex $\chi(R)$.

A very important thing to notice about $\chi(R)$ is that the R positions of the peaks are shifted to lower R from what $g(R)$ would give. For FeO, the first main peak occurs at 1.6 Å, while the FeO distance in FeO is more like 2.1 Å. This is not an error, but is due to the scattering phase-shift—recall that the EXAFS goes as $\sin[2kR + \delta(k)]$. As can be seen from the phase shifts shown in Figure 10, $\delta(k) \sim -k$ is a decent approximation of a typical phase-shift, which gives an apparent shift to the peaks in $\chi(R)$ of −0.5 Å or so.

The Fourier Transform results in a complex function for $\chi(R)$ even though $\chi(k)$ is a strictly real function. It is common to display only the magnitude of $\chi(R)$ as shown in solid in Figure 24, but the real (dashed) and imaginary components contain important information that cannot be ignored. When we get to the modeling the XAFS, it will be important to keep in mind that $\chi(R)$ has real and imaginary components, and we will model these, not just the magnitude.

The standard definition for a Fourier transform of a signal $f(t)$ can be written as

$$\tilde{f}(\omega) = \frac{1}{\sqrt{2\pi}} \int_{-\infty}^{\infty} f(t) e^{-i\omega t} dt$$

$$f(t) = \frac{1}{\sqrt{2\pi}} \int_{-\infty}^{\infty} \tilde{f}(\omega) e^{i\omega t} d\omega$$

where the symmetric normalization is one of the more common conventions. This gives Fourier

conjugate variables of ω and t, typically representing frequency and time, respectively. Because the XAFS equation (Eqn. 10) has $\chi(k) \propto \sin[2kR + \delta(k)]$, the conjugate variables in XAFS are generally taken to be k and $2R$. While the normalization for $\chi(R)$ and $\chi(k)$ is a matter of convention, we follow the symmetric case above (with t replaced by k and ω replaced by $2R$).

There are a few important modifications to mention for the typical use of Fourier transforms in XAFS analysis. First, an XAFS Fourier transform multiplies $\chi(k)$ by a power of k, typically k^2 or k^3, as shown in Figure 22. This weighting helps compensate for the strong decay with k of $\chi(k)$, and allows either emphasizing different portions of the spectra, or giving a fairly uniform intensity to the oscillations over the k range of the data. In addition, $\chi(k)$ is multiplied by a window function $\Omega(k)$ which acts to smooth the resulting Fourier transform and remove ripple and ringing that would result from a sudden truncation of $\chi(k)$ at the ends of the data range.

The second important issue is that the continuous Fourier transform described above is replaced by a discrete transform. This better matches the discrete sampling of energy and k values of the data, and allows Fast Fourier Transform techniques to be used, which greatly improves computational performance. Using a discrete transform does change the definitions of the transforms used somewhat. First, the $\chi(k)$ data must be interpolated onto a *uniformly spaced* set of k values. Typically, a spacing of $\delta k = 0.05$ Å^{-1} is used. Second, the array size for $\chi(k)$ used in the Fourier transform should be a power of 2, or at least a product of powers of 2, 3, and 5. Typically, $N_{\rm fft} = 2048$ points are used. With the default spacing between k points, this would accommodate $\chi(k)$ up to $k = 102.4$ Å^{-1}. Of course, real experimental data doesn't extend that far, so the array to be transformed is *zero-padded* to the end of the range.

The spacing of points in R is given as $\delta R = \pi/(N_{\rm fft}\delta k)$. The zero-padding of the extended k range will increase the density of points in $\chi(R)$ and result in smoothly interpolating the values. For $N_{\rm fft} = 2048$ and $\delta k = 0.05$ Å^{-1}, the spacing in R is approximately $\delta R \approx 0.0307$ Å. For the discrete Fourier transforms with samples of $\chi(k)$ at the points $k_n = n\delta k$, and samples of $\chi(R)$ at the points $R_m = m\delta R$, the definitions for the XAFS Fourier transforms become:

$$\tilde{\chi}(R_m) = \frac{i\delta k}{\sqrt{\pi N_{\rm fft}}} \sum_{n=1}^{N_{\rm fft}} \chi(k_n)\Omega(k_n) k_n^w e^{2i\pi nm/N_{\rm fft}}$$

$$\tilde{\chi}(k_n) = \frac{2i\delta R}{\sqrt{\pi N_{\rm fft}}} \sum_{m=1}^{N_{\rm fft}} \tilde{\chi}(R_m)\Omega(R_m) e^{-2i\pi nm/N_{\rm fft}}$$

This normalization convention preserves the symmetry properties of the Fourier Transforms with conjugate variables k and $2R$.

As mentioned above, the window function $\Omega(k)$ will smooth the resulting Fourier transform and reduce the amount of ripple that would arise from a sharp cut-off $\chi(k)$ at the ends of the data range. Since Fourier transforms are used widely in many fields of engineering and science, there is an extensive literature on such window functions, and a lot of choices and parameters available for constructing windows. In general terms, $\Omega(k)$ will gradually increases from 0 to 1 over the low-k region, and decrease from 1 to 0 over the high-k region, and may stay with a value 1 over some central portion. Several functional forms and parameters for these windows can be used, and are available in most EXAFS analysis software. Many good examples of the shapes, parameters, and effects of these on the resulting $\chi(R)$ are available in program documentation, and other on-line tutorials.

In many analyses, the inverse Fourier transform is used to select a particular R range and transform this back to k space, in effect *filtering* out most of the spectrum, and leaving only a narrow band of R values in the resulting filtered $\chi(k)$. Such filtering has the potential advantage of being able to isolate the EXAFS signal for a single shell of physical atoms around the

absorbing atom, and was how many of the earliest EXAFS analyses were done. This approach should be used with caution since, for all but the simplest of systems, it can be surprisingly difficult to effectively isolate the EXAFS contribution from an individual scattering atom this way. It is almost never possible to isolate a second neighbor coordination sphere in this way. For this reason, many modern analyses of EXAFS will use a Fourier transform to convert $\chi(k)$ to $\chi(R)$, and use $\chi(R)$ for data modeling, not bothering to try to use a filter to isolate shells of atoms.

XAFS DATA MODELING

In this section, we'll work through an example of a structural refinement of EXAFS. The FeO data shown and reduced in the previous section will be analyzed here. Of course, we know the expected results for this system, but it will serve to demonstrate the principles of XAFS modeling and allow us to comment on a number of subtleties in data modeling.

FeO has a simple rock salt structure, with Fe surrounded by 6 O, with octahedral symmetry, and then 12 Fe atoms in the next shell. Starting with this simple structure, we can calculate scattering amplitudes $f(k)$ and phase-shifts, $\delta(k)$ theoretically. A complete description of this calculation is beyond the scope of this treatment, but a few details will be given below. Once we have these theoretical scattering factors, we can use them in the EXAFS equation to refine structural parameters from our data. That is, we'll use the calculated functions $f(k)$ and $\delta(k)$ (and also $\lambda(k)$) in the EXAFS equation to predict the $\chi(k)$ and modify the structural parameters R, N, and σ^2 from Equation (10), and also allow E_0 (that is, the energy for which $k = 0$) to change until we get the best-fit to the $\chi(k)$ of the data. Because of the availability of the Fourier transform, we actually have a choice of doing the refinement with the measured $\chi(k)$ or with the Fourier transformed data. Working in R-space allows us to selectively ignore higher coordination shells, and we will use this approach in the examples here. When analyzing the data this way, the full complex XAFS $\chi(R)$, not just the magnitude $|\chi(R)|$, must be used.

The examples shown here are done with the FEFF (Rehr et al. 1991) program to construct the theoretical factors, and the IFEFFIT (Newville 2001a) package to do the analysis. Some aspects of the analysis shown here may depend on details of these particular programs, but similar results would be obtained with any of several other EXAFS analysis tools.

Running and using FEFF for EXAFS calculations

In order to calculate the $f(k)$ and $\delta(k)$ needed for the analysis, the FEFF program (Rehr et al. 1991) starts with a cluster of atoms, builds atomic potentials from this, and simulates a photoelectron with a particular energy being emitted by a particular absorbing atom and propagating along a set of scattering paths (Newville 2001b). FEFF represents a substantial work of modern theoretical condensed matter physics, and includes many effects that are conceptually subtle but quantitatively important, including the finite size of the scattering atoms, and many-body effects due to the fact that electrons are indistinguishable particles that must satisfy Pauli's exclusion principle (Rehr and Albers 2000). The details of these effects are beyond the scope of this work.

We do not, as may have been inferred from some of the earlier discussion, use FEFF to calculate $f(k)$ and $\delta(k)$ for the scattering of, say, an oxygen atom, and use that for all scattering of oxygen. Instead, we use FEFF to calculate the EXAFS for a particular path, say Fe-O-Fe taken from a realistic cluster of atoms. This includes the rather complex propagation of the photoelectron out of the Fe atom, through the sea of electrons in an iron oxide material, scattering from an oxygen atom with finite size, and propagating back to the absorbing Fe atom. As a result of this, we use FEFF to calculate the EXAFS for a particular set of paths so that we may then *refine* the path lengths and coordination numbers for those paths.

Starting with a cluster of atoms (which does not need to be crystalline, but this is often easy to use), FEFF determines the important scattering paths, and writes out a separate file for the scattering contributions for the EXAFS from each scattering path. Conveniently (and though it does not calculate these factors individually), it breaks up the results in a way that can be put into the standard form of the EXAFS equation (Eqn. 10), even for multiple-scattering paths. This allows analysis procedures to easily refine distances, apply multiplicative factors for coordination numbers and S_0^2, and apply disorder terms. Because the outputs are of a uniform format, we can readily mix outputs from different runs of the programs, which is important for modeling complex structures with multiple coordination environments for the absorbing atom.

First-shell fitting

For an example of modeling EXAFS, we start with FeO, a transition metal oxide with the particularly simple rock-salt structure, while still being representative of many systems found in nature and studied by EXAFS, in that the first shell is oxygen, and the second shell is a heavier metal element. We begin with modeling the first Fe-O shell of FeO, take a brief diversion into the meaning and interpretation of the statistical results of the modeling, and then continue on to analyze the second shell.

We start with the crystal structure, generate the input format for FEFF, run FEFF, and gather the outputs. For the rock-salt structure of FeO with six Fe-O near-neighbors in octahedral coordination, and twelve Fe-Fe second neighbors, there will be one file for the six Fe-O scattering paths, and one file for the twelve Fe-Fe scattering paths. To model the first shell EXAFS, we use the simulation for the Fe-O scattering path, and refine the values for NS_0^2, R, and σ^2. We set S_0^2 to 0.75. We will also refine a value for E_0, the threshold defining where k is 0. This is usually necessary because the choice of E_0 from the maximum of the first derivative of the spectra is *ad hoc*, and because the choice of energy threshold in the calculation is somewhat crude. Even if the refined value for E_0 does not change very much, it is strongly correlated with R, so that getting both its value and uncertainty from the fit is important.

The results of the initial refinement is shown in Figure 25, with best values and estimated uncertainties for the refined parameters given in Table 1. These values are not perfect for crystalline FeO, especially in that the distance is contracted from the expected value of 2.14 Å, but they are reasonably close for a first analysis.

It is instructive to look at this refinement more closely, and discuss a few of the details. The refinement was done on the data in R-space, after a Fourier transform of $k^2\chi(k)\Omega(k)$, where $\Omega(k)$ represents a Hanning window with a range between k = [2.5,13.5] Å^{-1}, and with a dk parameter of 2 Å^{-1}. The refinement used the real and imaginary components of $\chi(R)$ between R = [0.9, 2.0] Å. $k^2\chi(k)$ for the data and best-fit model, as well as $\Omega(k)$ are shown on the left side of Figure 26.

From Figures 25 and 26, it is evident that the higher frequency components (that is, from the second shell of Fe-Fe) dominate $k^2\chi(k)$. This is a useful reminder of the power of the Fourier transform in XAFS analysis: it allows us to concentrate on one shell at a time and ignore the others, even if they have larger overall amplitude.

Table 1. Best values and uncertainties (in parentheses) for the refined first shell parameters for FeO. The refinement fit the components of $\chi(R)$ between R = [0.9,2.0] Å after a Fourier transform using k = [2.5,13.5] Å^{-1}, a k-weight of 2, and a Hanning window function. S_0^2 was fixed to 0.75.

Shell	N	R (Å)	σ^2 (Å^2)	ΔE_0 (eV)
Fe-O	5.5(0.5)	2.10(0.01)	0.015(.002)	−3.2(1.0)

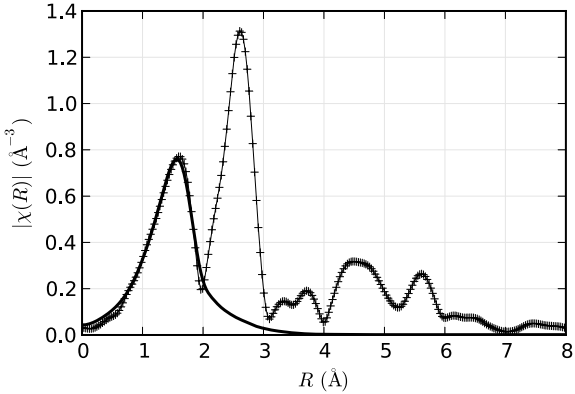

Figure 25. First shell fit to the EXAFS of FeO, showing the magnitude of the Fourier transform of the EXAFS, $|\chi(R)|$, for data (+) and best fit model (solid).

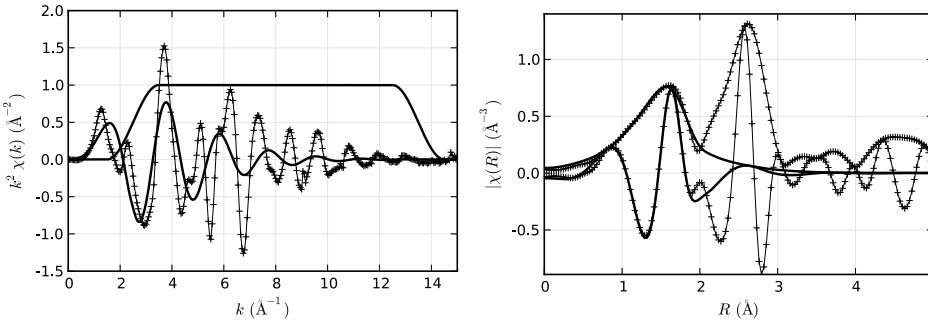

Figure 26. EXAFS $k^2\chi(k)$ (left) for data (+) and best-fit model (solid) for the first shell of FeO, and the window function, $\Omega(k)$, used for the Fourier transform to $\chi(R)$. While the solid curve shows the best-fit to the 1st shell of the EXAFS, this is not obvious from $k^2\chi(k)$. On the right, the real and magnitude components of $\chi(R)$ for the data (+) and best-fit model (solid) show that the model matches the data for the first shell very well.

Fit statistics and estimated uncertainties

At this point, we should pause to discuss further details of the fit, including the fit statistics and how the best-fit values and uncertainties are determined in the refinement. Because the EXAFS equation is complex, and non-linear in the parameters we wish to refine, the refinement is done with a non-linear least-squares fit. Such a fit uses the standard statistical definitions for chi-square and least-squares to determine the best values for the set of parameters varied as those values that give the smallest possible sum of squares of the difference in the model and data. The standard definition of the chi-square or χ^2 statistic (note the use of χ^2 from standard statistical treatments—don't confuse with the EXAFS χ!) that is minimized in a least-squares fit is defined as

$$\chi^2 = \sum_i^{N_{\text{data}}} \frac{[y_i^{\text{data}} - y_i^{\text{model}}(x)]^2}{\varepsilon^2}$$

where y_i^{data} is our experimental data, $y_i^{\text{model}}(x)$ is the model which depends on the variable fitting parameters x, N_{data} is the number of points being fit, and ε is uncertainty in the data. Each of these terms deserves more discussion.

The set of variable parameters x are the values actually changed in the fit. If we had fixed a value (say, for N), it would not be a variable. Below, we will impose relationships between parameters in the EXAFS equation, for example, using a single variable to give the value for E_0 for multiple paths. This counts as one variable in the fit, even though it may influence the value of several physical parameters for multiple paths in the model function.

Importantly, the χ^2 definition does not actually specify what is meant by the data y. In the fit above, we used the real and imaginary components of $\chi(R)$, after Fourier transforming the data with a particular window function and k-weight. Using different parameters for the transform would result in different data (and model) to be fit, and could change the results. We could have tried to fit the $k^2\chi(k)$ data without Fourier transforming, but as can be seen from Figure 26, the fit would likely have been substantially worse. But, as we are at liberty to decide what is meant by "the data" to be modeled, we can select the portion of the spectra we're most interested in, including changing the weighting parameters and windows. We can also use multiple spectra that we wish to model with one set of parameters x as "the data." Of course, any transformation or extensions we make to the data must be applied equally to the model for the data. In general, we find that fitting EXAFS data in R-space strikes a good balance between not changing the data substantially, and allowing us to select the k and R ranges we wish to and are able to model.

The uncertainty in the data is represented by ε in the above definition for χ^2. Of course, this too must match what we mean by "the data," and will generally mean the uncertainty in $\chi(R)$ in the range of the data we're modeling. There are many general strategies for estimating uncertainties in data, usually based on involved statistical treatment of many measurements. Such efforts are very useful, but tend to be challenging to apply for every EXAFS spectra. A convenient if crude approach is to rely on the fact that EXAFS decays rapidly with R and to assert that the data at very high R (say, above 15 Å) reflects the noise level. Applying this to the R range of our data assumes that the noise is independent of R (white noise), which is surely an approximation. The advantage of the approach is that it can be applied automatically for any set of data. Tests have shown that it gives a reasonable estimate for data of low to normal quality, and underestimates the noise level for very good data. A simple relationship based on Parseval's theorem and Fourier analysis can be used to relate ε_R, the noise estimate in $\chi(R)$ to ε_k, the noise in $\chi(k)$ (Newville et al. 1999).

There are two additional statistics that are particularly useful (Lytle et al. 1989). One of these is the reduced chi-square, defined as $\chi^2_\nu = \chi^2/(N_{\mathrm{data}} - N_{\mathrm{varys}})$ where N_{varys} is the number of variable parameters in the fit. This has the feature of being a measure of goodness-of-fit that is takes into account the number of variables used. In principle, for a good fit and data with well-characterized uncertainties, ε, this value should approach 1. χ^2_ν is especially useful when comparing whether one fit is better than another. In simplest terms, a fit with a lower value for χ^2 is said to be better than one with a higher value, even if the two fits have different number of variables. Of course, there is some statistical uncertainty in this assertion, and confidence intervals and F tests can be applied to do a more rigorous analysis. For EXAFS analysis, a principle difficulty is that the values of χ^2_ν are often several orders of magnitude worse than 1, far worse than can be ascribed to a poor estimate of ε. Partly because of this, another statistic is $\mathcal{R}$, or R-factor, defined as

$$\mathcal{R} = \frac{\sum_i^{N_{\mathrm{data}}}[y_i^{\mathrm{data}} - y_i^{\mathrm{model}}(x)]^2}{\sum_i^{N_{\mathrm{data}}}[y_i^{\mathrm{data}}]^2}$$

which gives the size of the misfit relative to the norm of the data. This value is typically found to below 0.05 or so for good fits, and is often found to be much better than that.

Last, and possibly most surprising for the discussion of the pieces in the definition of χ^2, we come to the problem of identifying N_{data}. When measuring $\mu(E)$ we are free to sample as many energy points as we wish, but increasing the number of points in $\mu(E)$ over a particular energy range doesn't necessarily mean we have a better measure of the first shell EXAFS. That is, the EXAFS oscillations are relatively slow in energy, and sampling $\mu(E)$ at 0.1 eV steps over the EXAFS range does not give a better measurement of the first shell EXAFS than acquiring for the same total time but sampling at 1 eV steps. In the previous chapter, we mentioned that the zero-padding and fine spacing of k data sets the spacing of data in R. We should be clear that this can (and usually does) greatly over-sample the data in R space. Oversampling is not bad—it generally improves stability—but it must be understood that it is not adding new, independent data.

For any waveform or signal, the Nyquist-Shannon sampling theorem tells us that the maximum R that can be measured is related to the spacing of sampled data points in k, according to (for EXAFS, with conjugate Fourier variables of k and $2R$):

$$R_{max} = \frac{\pi}{2\delta k}$$

where R_{max} is the maximum R value we can detect, and δk is the spacing for the $\chi(k)$ data. Using $\delta k = 0.05$ Å^{-1} is common in EXAFS, which means we cannot detect EXAFS contributions beyond 31.4 Å. As the converse of this, the resolution for an EXAFS spectrum – the separation in R below which two peaks can be independently measured—is given as

$$\delta R = \frac{\pi}{2k_{max}}$$

where k_{max} is the maximum measured value of k. In short, what matters most for determining how well $\chi(R)$ is measured for any particular value of R is how many periods of oscillations there are in $\chi(k)$.

Related to both R_{max} and the resolution δR, and also resulting from basic signal processing theory and Fourier analysis, the number of independent measurements in a band-limited waveform is

$$N_{ind} \approx \frac{2\Delta k \Delta R}{\pi} + 1 \tag{12}$$

where Δk and ΔR are the range of useful data in k and R. For completeness, the above equation is often given with a "+2" instead of a "+1"(Stern 1993) in the EXAFS literature, though we will follow the more conservative estimate, and note that it would give an upper limit on the number of variables that could be determined from a set of noise-free data. No matter whether "+1" or "+2" is used, the main point is that number of data points available over a particular range of R is given by range of data in k. Making measurements with extremely fine steps in k (or energy) will allow data at higher R to be reliably modeled, but it does allow more parameters to be determined over a particular range of R below R_{max}. In order to be able to fit more parameters over a particular range of R, data needs to be collected to higher k.

Thus, we should modify the definition of χ^2 (and χ^2_ν) used to reflect the number of truly independent data points in the data, as

$$\chi^2 = \frac{N_{ind}}{N_{data}} \sum_i^{N_{data}} \frac{[y_i^{data} - y_i^{model}(x)]^2}{\varepsilon^2} \tag{13}$$

where N_{ind} is given by Equation (12) and N_{data} is the number of samples used for the data, even if this far exceeds N_{ind}. Values of N_{ind} for real EXAFS data are not very large. In the first

shell fit to FeO, we used k = [2.5,13.5] Å^{-1} and R = [0.9,2.0] Å which gives $N_{ind} \approx 8.7$, and we used 4 variables in the fit—roughly half the maximum. For higher shells and more complicated structures, we will have to come up with ways to limit the number of variables in fits in order to stay below the number of independent measurements for any particular R range that the data actually can support.

Estimates of the uncertainties for variables and correlations between pairs of variables can be made by measuring how χ^2 changes as variables are moved away from their best-fit values. Standard statistical arguments indicate that 1σ error bars (that indicate a 68% confidence in the value) should increase χ^2 by 1 from its best-fit value. This assumes that $\chi^2_\nu \approx 1$, which is usually not true for EXAFS data. As a consequence, it is common in the EXAFS literature to report uncertainties for values that increase χ^2 by χ^2_ν. This is equivalent to asserting that a fit is actually good, and scaling ε so that χ^2_ν is 1.

The estimation of uncertainties and correlations between variables can be very fast, as the computational algorithms used for minimization compute intermediate values related to the correlations between variables (in the form of the covariance matrix) in order to find the best values. Uncertainties determined this way include the effect of correlations (that is, moving the value for one variable away from its best value may change what the best value for another variable would be), but also make some assumptions about how the values of the variable interact. More sophisticated approaches, including brute-force exploration of values by stepping a variable through a set of values and repeatedly refining the rest of the variables, can give better measures of uncertainties, but are more computationally expensive.

Though the aim of a fit is to find the best values for the fitting parameters x, the computational techniques used do not guarantee that the "global" minimum of χ^2 is found, only that a "local" minima is found based on the starting values. This, of course, can cause considerable concern. Care should be taken to check that the results found are not too sensitive to the starting values for the variables or data manipulation parameters including Fourier transform ranges and weights, and background subtraction parameters. Checking for false global minima is somewhat more involved. Fortunately, for EXAFS analysis with reasonably well-defined shells, false minima usually give obviously non-physical results, such as negative or huge coordination numbers or negative values for σ^2. Another warning sign for a poor model is an E_0 shift away from the maximum of the first derivative by 10 eV or more. This can sometimes happen, but it might also indicate that the model $\chi(k)$ may have "jumped" a half or whole period away from its correct position, and that the amplitude parameters may be very far off, as if the Z for the scatterer is wrong.

Our diversion into fitting statistics is complete, and we can return to our first shell fit to Fe-O before continuing on. The data was estimated to have $\varepsilon_R \approx 5 \times 10^{-3}$ and $\varepsilon_k \approx 2 \times 10^{-4}$, which is a typical noise level for experimental $\chi(k)$ data. With a standard k grid of 0.05 Å^{-1}, and an R grid of ≈ 0.0307 Å, the fit had 72 data points, but $N_{ind} \approx 8.7$. Scaled to N_{ind} as in Equation (13), the fit has $\chi^2 \approx 243$ and $\chi^2_\nu \approx 51.7$ (again with 4 variables), and $\mathcal{R} \approx 0.005$.

Second-shell fitting

We are now ready to include the second shell in the model for the FeO EXAFS. To do this, we simply add the path for Fe-Fe scattering to the sum in the EXAFS equation. We will add variables for R, N, and σ^2 for the Fe-Fe shell to those for the Fe-O scattering path. We'll use the same value for E_0 for both the Fe-O and Fe-Fe path, and keep all parameters the same as for the fit above, except that we'll extend the R range to be R = [0.9,3.1] Å. This will increase N_{ind} to ≈ 15.7, while we've increased the number of variables to 7.

The fit is shown in Figure 27 and values and uncertainties for the fitted variables are given in Table 2. The fit gave statistics of $\chi^2 \approx 837$, $\chi^2_\nu \approx 96$, and $\mathcal{R} \approx 0.0059$. The structural

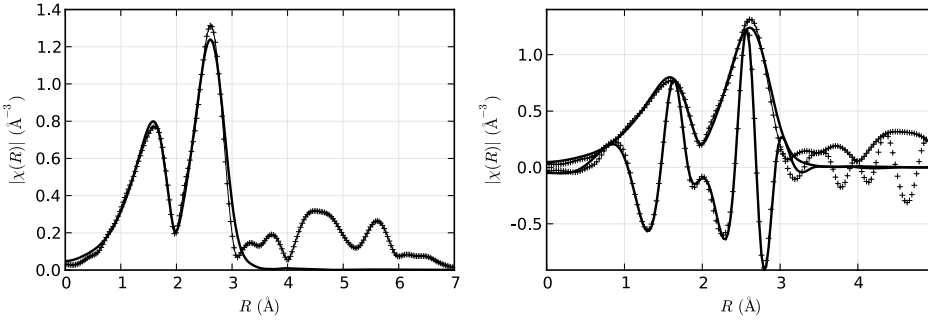

Figure 27. EXAFS $|\chi(R)|$ (left) and $Re[\chi(R)]$ (right) for FeO data (+) and best-fit model (solid) for the first two shells around Fe, including Fe-O and Fe-Fe scattering paths.

Table 2. Best values and uncertainties (in parentheses) for the refined first (Fe-O) and second (Fe-Fe) shells for FeO. The refinement fit the components of $\chi(R)$ between R = [0.9,3.0] Å with all other parameters as in Table 1.

Shell	***N***	***R*** **(Å)**	σ^2 **(Å²)**	ΔE_0 **(eV)**
Fe-O	5.3(0.5)	2.11(0.01)	0.013(.002)	−1.2(0.5)
Fe-Fe	13.4(1.3)	3.08(0.01)	0.015(.001)	−1.2(0.5)

values for distances and coordination number are consistent with the known crystal structure of FeO, though the Fe-O distance is a bit shorter than expected, and the Fe-Fe is a bit longer than expected, both suggesting that there may be some contamination of a ferric iron phase in the sample. The fits are shown in Figure 27, and individual contributions to the total best-fit spectrum are shown in both *k*- and *R*-space in Figure 28.

An important aspect of using fitting techniques to model experimental data is the ability to compare different fits to decide which of two different models is better. We will illustrate this by questioning the assumption in the above the model that the E_0 parameter should be exactly the same for the Fe-O and Fe-Fe scattering path. Changing this model to allow another variable parameter and re-running the fit is straightforward. For this data set, the fit results are close enough to the previous fit that the graphs of $\chi(k)$ and $\chi(R)$ are nearly unchanged. The newly refined values for the parameter are given in Table 3. Compared to the values in Table 2, the results are very similar except for the values of E_0 and a slight increase in uncertainties.

The fit statistics for this refinement are $\chi^2 \approx 811$, $\chi^2_\nu \approx 105$, and $\mathcal{R} \approx 0.0057$. Since both χ^2 and $\mathcal{R}$ have decreased, the model with 2 independent E_0 values is clearly a closer match to the data. However, we added a variable to the model, so it is reasonable to expect that the fit should be better. But is the fit sufficient to justify the additional variable? The simplest approach to answering this question is to ask if χ^2_ν has improved. In this case, it has not—it went from roughly 96 to 105. Since these statistics all have uncertainties associated with them, a slightly more subtle question is: what is the probability that the second fit is better than the first? A standard statistical *F*-test can be used to give this probability, which turns out to be about 32% for these two fits (that is, with $N_{\rm ind} = 15.7$, $\chi^2 \approx 837$ for 8 variables and $\chi^2 \approx 811$ for 7 variables).

Another way to look at this is to ask if the added variable (E_0 for the Fe-Fe shell) found a value that was significantly different from the value it would have otherwise had. The two values for E_0 in the "2 E_0 model" are noticeably different from one another—approximately at the limits of their uncertainties—but both are consistent with the value found in the "1 E_0 model."

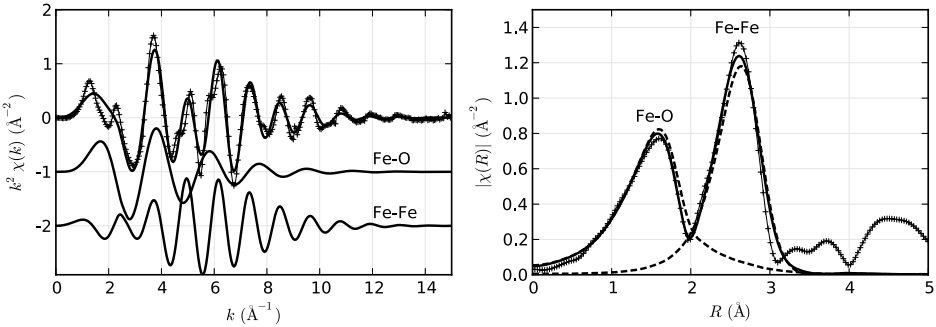

Figure 28. Contributions of the first and second shell to the total model fit to the FeO EXAFS. On the left, the fit (solid) matches the data (+) much better than in Figure 26. Note that, compared to the Fe-O contribution the Fe-Fe contribution has a shorter period corresponding to longer interatomic distance, and has magnitude centered at higher k, as predicted by the $f(k)$ function shown in Figure 10. On the right, the $|\chi(R)|$ of the contributions from the two shells are shown. Though there is a sharp dip at 2 Å between peaks for the two shells, there is substantial leakage from one shell to another.

Table 3. Best values and uncertainties (in parentheses) for the refined first (Fe-O) and second (Fe-Fe) shells for FeO for a model just like that shown in Table 2 except that the 2 values for E_0 are allowed to vary independently.

Shell	N	R (Å)	σ^2 (Å^2)	ΔE_0 (eV)
Fe-O	5.3(0.6)	2.12(0.01)	0.013(.002)	−0.7(1.2)
Fe-Fe	13.3(1.3)	3.08(0.01)	0.015(.001)	−1.5(0.8)

This also leads us to the conclusion that the additional variable E_0 is not actually necessary for modeling this data.

We've seen that structural refinement of EXAFS data can be somewhat complicated, even for a relatively straightforward system such as FeO. Many real systems can be much more challenging, but the fundamental principles described here remain the same. The ability to alter which of the physical parameters describing the different paths in the EXAFS sum are independently varied in the refinement, and test the robustness of these, can be especially important for more sophisticated analysis. One way to think about this is that in the first version of the above example, we used the value of one variable for two different path variables—E_0 for the Fe-O and Fe-Fe paths, and then demonstrated that using one value for these two physical parameters was robust. This is the simplest type of constraint that can be applied in an EXAFS analysis. In this case, it has the noticeable advantage of improving the fit because it uses fewer independent variables. For a mixed coordination shell, perhaps a mixture of Fe-O and Fe-S, one may want to include paths for Fe-O and Fe-S and ask the model not to simply refine the weight of each of these independently but rather to ask what fraction of the Fe atoms are coordinated by oxygen. To do this, one would vary the fraction x_{FeO} as a pre-factor to the amplitude term for the Fe-O path and constrain the coordination number for the Fe-S path to use $1 - x_{\mathrm{FeO}}$. More complex constraints can be imposed when simultaneously refining data from different edges or different temperatures measured on the same sample. In a sense, the use of multiple paths for different parts of the R range for $\chi(R)$ in the fit above is merely the starting point for thinking about how different contributions can be put together to make a model for a set of data.

The basic formalism for modeling EXAFS data has been given, based on the Path expansion, theoretical calculations of the contributions for these paths, the Fourier transform,

and a statistical understanding of the information present in a real EXAFS spectrum. We have illustrated a simple approach to refining a structural model using EXAFS data, and used statistical methods to compare two different candidate models. Finally we have outlined the route forward to building models for more complex EXAFS data.

Two distinct and essential challenges exist for EXAFS analysis. First, the complexity of the theoretical calculations for photoelectron scattering make it difficult to get scattering factors $f(k)$ and $\delta(k)$ that can match the accuracy of measured EXAFS data. By itself, this has proven to not be a serious problem, as the EXAFS literature is full of examples showing the accuracy of the results from EXAFS despite the imperfect theoretical calculations. Second, the limited information contained in a finite EXAFS spectrum coupled with the number of scattering paths needed to model real systems makes building and testing realistic models for complex systems challenging. Progress in analysis tools for EXAFS continues to make the building and testing of such models easier and more robust, but modeling still requires a fair amount of expertise and care. Despite the challenges, EXAFS has been proven to give reproducible and reliable measures of the local structure around selected atoms that cannot be obtained in any other way, and the number of scientists using EXAFS in both mature and new fields of science continues to grow.

REFERENCES

Als-Nielsen J, McMorrow D (2001) Elements of Modern X-ray Physics. John Wiley & Sons

Booth CH, Bridges F (2005) Improved self-absorption correction for fluorescence measurements of extended X-ray absorption fine-structure. Physica Scripta T115:202-204

Brown GE, Calas G, Waychunas GA, Petiau J (1998) X-ray absorption spectroscopy; applications in mineralogy and geochemistry. Rev Mineral Geochem 18:431-512

Bunker G (2010) Introduction to XAFS: A Practical Guide to X-ray Absorption Fine Structure Spectroscopy. Cambridge University Press

Calvin S (2013*)* XAFS for Everyone. CRC Press

Filipponi A, Di Cicco A, Natoli CR (1995) X-ray-absorption spectroscopy and n-body distribution functions in condensed matter. Phys Rev B 52:15122–15134

IXAS (2012) International X-ray Absorption Society. *http://www.ixasportal.net/*

Kelly SD, Hesterberg D, Ravel B (2008) Analysis of Soils and Minerals using X-ray Absorption Spectrocopy. *In:* Methods of Soil Analysis Part 5 - Mineralogical Methods. Ulery AL, Drees LR (eds), Soil Science Society of America, p 387-464

Koningsberger DC, Prins R (eds) (1998) X-ray Absorption: Principles, Applications, Techniques of EXAFS, SEXAFS, and XANES. John Wiley & Sons

Lytle FW, Sayers DE, Stern EA (1989) Report on the international workshop on standards and criteria in x-ray absorption spectroscopies. Physica B 158:701-722

Manceau A, Marcus MA, Tamura N (2002) Quantitative speciation of heavy metals in soils and sediments by synchrotron X-ray techniques. Rev Mineral Geochem 49:341-428

Newville M (2001a) IFEFFIT: interactive XAFS analysis and FEFF fitting. J Synchrotron Radiat 8:322-324

Newville M (2001b) EXAFS analysis using FEFF and FEFFIT. J Synchrotron Radiat 8:96-100

Newville M, Livins P, Yacoby Y, Rehr JJ, Stern EA (1993) Near-edge X-ray-absorption fine structure of Pb: A comparison of theory and experiment. Phys Rev B 47:14126-14131

Newville M, Boyanov B, Sayers DE (1999) Estimation of uncertainties in XAFS data. J Synchrotron Radiat 6:264-265

Pfalzer P, Urbach JP, Klemm M, Horn S, denBoer ML, Frenkel AI, Kirkland JP (1999) Elimination of self-absorption in fluorescence hard-x-ray absorption spectra. Phys Rev B 60:9335-9339

Ravel B, Newville M (2005) ATHENA, ARTEMIS, HEPHAESTUS: data analysis for X-ray absorption spectroscopy using IFEFFIT. J Synchrotron Radiat 12:537-541

Rehr JJ, Albers RC (2000) Theoretical approaches to x-ray absorption fine-structure. Rev Mod Phys 72(3):621-654

Rehr JJ, Mustre de Leon J, Zabinsky SI, Albers RC (1991) Theoretical X-ray absorption fine structure standards. J Am Chem Soc 113:5135-5140

Stern EA (1988) Principles of EXAFS. *In:* X-ray Absorption: Principles, Applications, Techniques of EXAFS, SEXAFS, and XANES. Koningsberger DC, Prins R (eds) John Wiley & Sons, Chapter 1

Stern EA (1993) Number of relevant independent points in x-ray-absorption fine-structure spectra. Phys Rev B 48:9825-9827

Stern EA, Heald SM (1983) Principles and Applications of EXAFS. *In:* Handbook of Synchrotron Radiation. Koch EE (ed) North-Holland, p 995-1014

Sutton SR, Bertsch PM, Newville M, Rivers M, Lanzirotti A, Eng P (2002) Microfluorescence and microtomography analyses of heterogeneous earth and environmental materials. Rev Mineral Geochem 49:429-483

Teo BK (1986) EXAFS: Basic Principles and Data Analysis. Springer-Verlag

XAFS.ORG (2003) *http://xafs.org* {Site as of 2013 will be: *http://www.ixasportal.net/wiki/doku.php*}